INVESTIGATING CELL AND TISSUE MECHANICS DURING *DROSOPHILA* EMBRYOGENESIS USING LASER MICROSURGERY

By

Holley E. Lynch

Dissertation

Submitted to the Faculty of the

Graduate School of Vanderbilt University

in partial fulfillment of the requirements

for the degree of

DOCTOR OF PHILOSOPHY

in

Physics

December, 2012

Nashville, TN

Approved:

Professor M. Shane Hutson

Professor John P. Wikswo Jr.

Professor Chris J. Janetopoulos

Professor Volker E. Oberacker

Professor Kalman Varga

To my family,

thanks for your continuing belief and support as I pursue my dreams.

ACKNOWLEDGEMENTS

This dissertation would not have been possible without the generous support of many people. First and foremost, I want to thank my advisor M. Shane Hutson for his guidance throughout my time at Vanderbilt. He encouraged me to take advantage of many opportunities during my time here, including presenting my work at a conference in Japan. He has also tirelessly worked to encourage us to become better scientific writers. I hope some of it stuck.

I would also like to thank the rest of my committee members for their advice and guidance. This dissertation would not be what it is without all of your feedback and encouragement.

I appreciate all of the support I received from past and present group members. All of you have listened to my 'crazy ideas' and 'stupid questions' with patience and advice. Without training from Xiaoyan Ma none of this research would have been done. I would also like to thank Sarah Crews, not only for kindly proof reading my dissertation, but also for the countless times she encouraged me to go ahead and hit the send button. Without the assistance of David Mashburn, I would still be segmenting cells. Aroshan Jayasinghe and I have shared an office since the beginning of my time at Vanderbilt. Whenever I was stuck on a problem, be it classwork or research, I knew I simply had to turn my chair and ask for assistance. Thank you.

I am grateful for all of the support I received from G. Wayne Brodland's group at the University of Waterloo. Not only did they provide me with the software I used to

model cell sheets, but their quick responses to my emails and the wonderful brainstorming in the weekly skype meetings were extremely helpful.

I would also like to thank the undergraduate researchers who came through our lab. Brett Rosenthal performed the line incisions on several of the germband segments and Elliott Kim and Robert Gish collected many of the control movies for germband retraction as well as designing and performing many of the amnioserosa cuts.

This work was funded through the National Science Foundation, National Institutes of Health, and the GAANN fellowship.

Last but not least, I would like to thank my parents for understanding when I needed to work long hours and when a timely delivery of food would be invaluable.

TABLE OF CONTENTS

Page

LIST OF TABLES

Table Page

LIST OF FIGURES

CHAPTER 1

INTRODUCTION

1.1 Motivation

Living tissues are interesting physical systems, behaving as active, non-linear viscoelastic materials. Their constituent cells act in a viscoelastic manner, sometimes acting more like a liquid and sometimes more like a solid. Interestingly, the *in vivo* physical properties of a particular cell type can change through development [1], as cells and tissues move across and through the embryo to form the precursors for adult organs and tissues. The mechanical properties of cells depend on their physical environment. Thus cells and tissues in culture often have different mechanical properties than those in living organisms. Even just changing the substrate on which cells are grown can affect their shape and cytoskeletal arrangement [2]. Therefore, changes through development in the mechanics of cells could result from changes in their physical environment, making development a rich and complicated physical system.

Development involves the dynamic, and often coordinated, motion of both tissues and cells. Assessing the mechanical interactions that lead to these motions is vital for a complete understanding. Although the genetic triggers for these motions are known in several cases, the actual forces and mechanical interactions involved remain largely unknown, and yet these processes can only be understood by considering both their biological and physical aspects. A good system for probing the physical aspects of

embryonic development is a system for which much of the genetics is already known, the common fruit fly *Drosophila melanogaster*.

We concentrate on two back-to-back stages of *Drosophila* embryonic development that involve the dynamic motion of two tissues across the surface of the embryo: germband retraction and dorsal closure. At 25°C, germband retraction begins around 7.5 hours after fertilization and dorsal closure ends about 6 hours later; the embryo hatches into a larva approximately 9 hours after dorsal closure ends [3]. Although much work has been done studying the relevant genetics for these stages, their mechanics are not yet fully understood. They also provide an accessible system to probe tissue and cell dynamics since the relevant tissues are on the surface of the embryo. For the earliest stage, germband retraction, I will focus on understanding the mechanical interactions between the amnioserosa and germband that allow them to move in concert to restore the tail of the developing tissue to the posterior of the embryo. In the following stage, dorsal closure, much work has been done to delineate the contributions of the tissues to the motion [4,5]. For this stage, I will focus on the mechanics of amnioserosa cells during their apical constriction.

Laser microsurgery provides the spatial and temporal control necessary to investigate the physical properties of both tissues and cells. On the tissue level, we use laser microsurgery to investigate the mechanical properties of individual segments of the germband and to design incisions that both test the necessity of various parts of the amnioserosa for retraction and allow us to separate its biochemical and mechanical contributions. On the cell level, laser hole-drilling can be used to elucidate the subcellular stress distribution during apical constriction of amnioserosa cells during dorsal closure.

Although laser microsurgery experiments give us powerful insights into the tissue mechanics of germband retraction and the tension distribution in amnioserosa cells during dorsal closure, only in combination with computational simulations can we create a complete model of the physics behind our experimental results. Thus, we combined laser microsurgery with a finite-element model to elucidate the mechanics of germband retraction and to discover the tension carrying mechanisms for apical constriction in the amnioserosa.

1.2 Overview

The next section of this chapter presents an overview of the biological system used to probe the mechanics of development, namely epithelial cells in *Drosophila* embryos during germband retraction and dorsal closure. It then discusses the relevant physics for studying and modeling this system. Section 1.4 then presents a detailed overview of the materials and methods used throughout this dissertation. The following three chapters discuss the results of my work on germband retraction and dorsal closure. Chapter 2 focuses on the mechanical interactions between the germband and amnioserosa necessary for germband retraction as determined by laser microsurgery. Chapter 3 then considers computer simulations of one important set of ablations in Chapter 2, using the simulations in conjunction with the results discussed in Chapter 2 to build a more complete model of germband retraction. These two chapters have not yet been published, but the manuscripts are in progress. In Chapter 4, we will leave both tissue-level mechanics and germband retraction to study the cell-level mechanics of amnioserosa

cells during dorsal closure (much is already known about the tissue mechanics at this stage). Specifically, we will investigate the carriers of tension in amnioserosa cells as they undergo apical constriction. The work in Chapter 4 represents my contributions to two publications [1,6]. Chapter 5 will then draw together the conclusions from the preceding three chapters.

1.3 Background

1.3.1 The System

1.3.1.1 Epithelial cells

The tissues involved in both germband retraction and dorsal closure are epithelial tissues. Epithelial cells, unlike other cell types, adhere to each other only on their lateral surfaces. Their basal surfaces adhere to an extracellular matrix (basal lamina) and their apical surface adheres to either other cell types, tissue fluids, or an extracellular matrix [7]. In the case of both germband and amnioserosa cells, their apical surface is exposed to the perivitelline fluid. Like other eukaryotic cells, epithelial cells consist of a nucleus surrounded by a cytoplasm, which is in turn surrounded by a plasma membrane (Figure 1.1). Though not by any means an exhaustive list of cell features, it is these base properties which influence the physical properties of a cell.

A system of filaments called the cytoskeleton exists throughout the cytoplasm. It is made of three fundamental types of filaments: intermediate filaments, microtubules, and actin filaments [8]. Intermediate filaments provide mechanical strength and

resistance to shear stress in the cell. Microtubules play a role in intracellular transport. Actin filaments determine the shape of the cell's surface and play a role in whole cell locomotion. A cell's cytoskeleton is quite dynamic, reorganizing as the cell's environment or needs change. Cytoskeletal filaments provide attachment sites for motor proteins, like myosin. There are several types of myosin, whose exact functions are not always known. Myosin I is involved in intracellular organization and the protrusion of actin-rich structures at the cell surface. Myosin II moves along actin filaments and is associated with contractile activity in both muscle and non-muscle cells [8]. Non-muscle myosin II is implicated in cell motility [9]. Both myosin I and II are found in both humans and *Drosophila* [8].

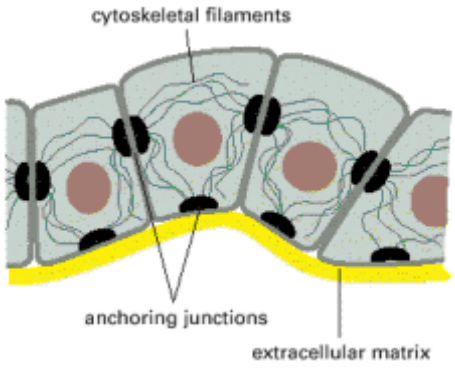

Figure 1.1. Schematic representation of epithelial cells. Pink represents the nucleus. Cell adhesion molecules are shown in black. Gray represents the plasma membrane. Light blue represents the cytoplasm. Cytoskeletal filaments and extracellular matrix are as labeled. Apical surface is towards the top and basal surface is against the extracellular matrix. Figure reproduced from [8].

Epithelial cells' plasma membranes allow interactions between each cell and its environment. These interactions are mainly conducted through transmembrane proteins, which can act as both receptors and adhesion molecules [7,8]. Cells often communicate with each other through secreted molecules that bind to receptors on the target cell, which then initiate that cell's response. Cell adhesion molecules also act as receptors, but in

addition to this role they bind a cell to its neighbors or the basal lamina (Figure 1.2). Adhesion molecules are divided into two categories: cell adhesion molecules and substratum adhesion molecules [7]. Three examples of cell adhesion molecules are cadherins, the immunoglobulin superfamily, and selectins. These bind cells to each other. Integrins are an example of substratum adhesion molecules. They bind cells to extracellular matrix proteins. Both catagories of adhesion molecules attach to the actin cytoskeleton inside the cell, and transmit cell-generated forces to other cells or the extracellular matrix [10]. Figure 1.2 shows several types of adhesive junctions in epithelial cells.

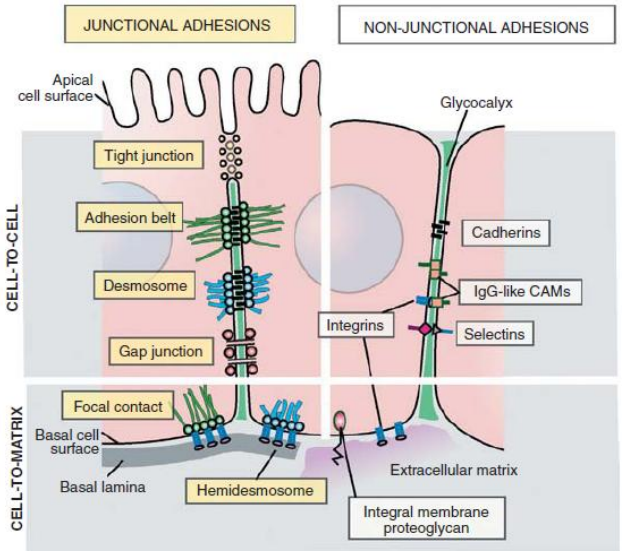

Figure 1.2. Schematic representation of several adhesion types between epithelial cells and their neighbors as well as those between the cells and the extracellular matrix. Figure reproduced from [7].

Localization of adhesion molecules polarizes epithelial cells. In many tissues, cells are polarized along their apical-basal axis by the localization of substratum adhesion molecules to the basal surface but not the apical surface. The cells illustrated in Figures 1.1 and 1.2 show apical-basal polarization. Localization of cell adhesion molecules can

also cause planar cell polarity, making cells more likely to adhere on one lateral surface than another. In general cell polarity involves non-symmetric localization of proteins along the surfaces of the cells, and can lead to morphogenetic change [7].

1.3.1.2 Drosophila embryos

Drosophila embryos are roughly ellipsoidal, measuring approximately 500 μm along their longest axis and 200 μm along their shortest. The interior of the embryo has a yolk sac that provides nutrients as it develops. The entire embryo is surrounded by two protective layers: the chorion and the vitelline membrane. The chorion is a hard shell that helps protect the embryo from damage. It is not optically transparent, but can be removed from the embryo without a loss in embryo shape. The vitelline membrane, an optically transparent membrane, is located inside the chorion and helps the embryo maintain its shape. Since the yolk creates a positive pressure on the vitelline, removing the membrane leads to a loss of shape [11] and without care leads to the destruction of the embryo. Between the vitelline membrane and the cell(s) of the embryo, there is a perivitelline fluid, which is an aqueous solution containing potassium, sodium, magnesium, calcium, chlorine, phosphorous, and sulfur ions [12].

The development of *Drosophila* embryos is temperature dependent and strain dependent. At 25°C an embryo hatches to a larva approximately 22 hours after fertilization [3]. All times that follow assume this temperature. *Drosophila* embryos begin as a single cell in which the nuclei divide eight times and begin to migrate to the surface. Once the nuclei reach the surface (approximately 2 hrs after fertilization), cell membranes in this synctium extend between the nuclei to form cells, a process known as cellularization [3]. After cellularization, embryos undergo gastrulation, where some cells

move interior to the embryo allowing for the eventual formation of organs and multiple cell levels. During gastrulation, surface epithelial cells known as germband cells begin to elongate. During the next two phases of development, the elongated germband cells intercalate, elongating the tissue perpendicular to their long axis in a process known as convergent extension. By the end of germband elongation (around 5.5 hours after fertilization), the germband will stretch across the ventral side of the embryo, around the embryo posterior, and onto the dorsal surface (top left frame of Figure 1.3).

1.3.1.3 Germband retraction

Around 7.5 hours after fertilization, the extended germband begins to retract [3]. Germband retraction last approximately 2-2.5 hours and is a stage defined by the dynamic coordinated movements of two tissues on the surface of the embryo: the germband and amnioserosa [13] (Figure 1.3 and 1.4). Figure 1.3 shows a time progression of germband retraction. As retraction begins, the germband covers most of the surface of the embryo stretching from the ventral surface around the posterior end and covering over half of the dorsal surface. The amnioserosa is mainly constrained to the two lateral surfaces of the embryo with only a small dorsal bridge connecting the two lateral flanks of tissue. The amnioserosa and germband then move together during retraction, maintaining neighbor contacts [13] as the germband shortens and unfurls until it is only on the ventral side. At the same time, the amnioserosa cells shorten and broaden until the amnioserosa inhabits a tear-drop shape on the dorsal surface of the embryo. Germband cells, especially in the rows closest to the amnioserosa, elongate towards the amnioserosa.

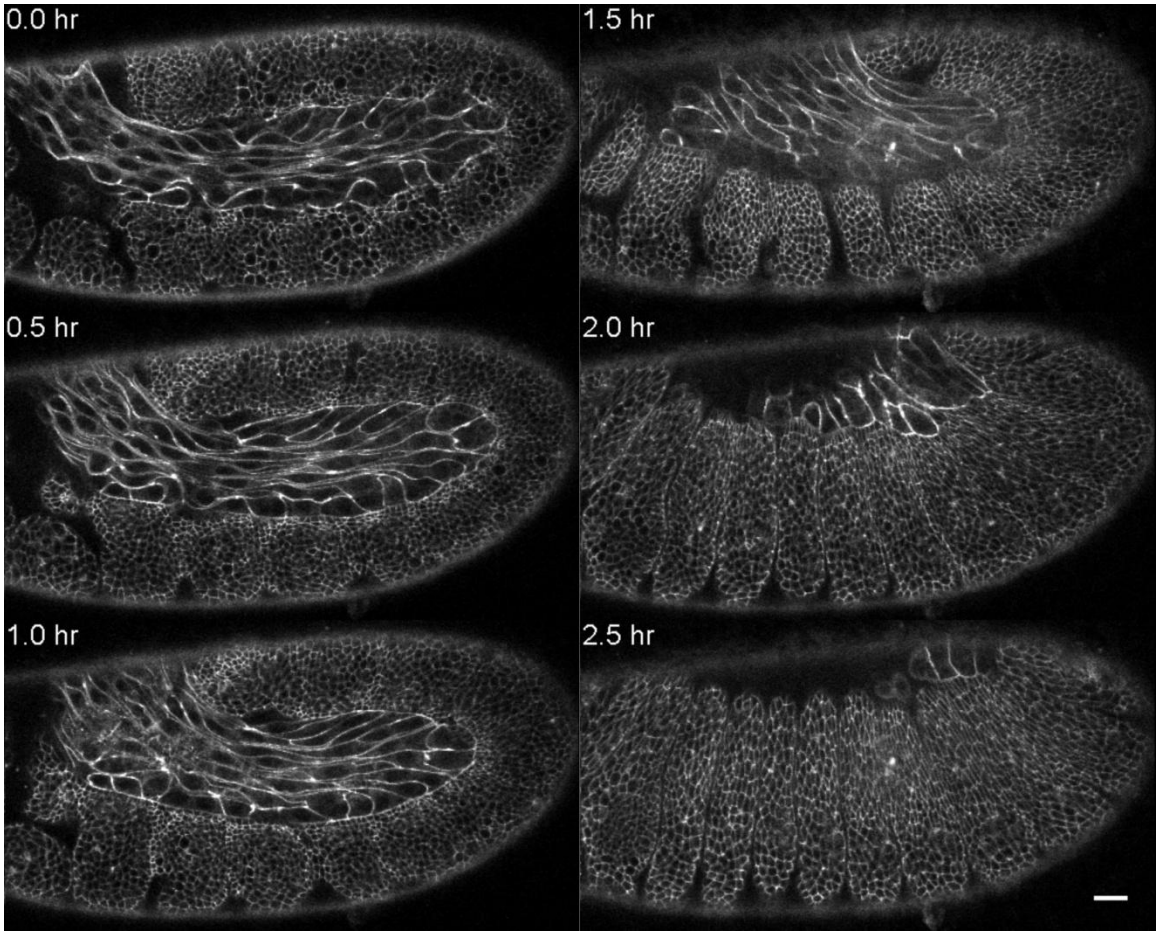

Figure 1.3. Time progression of germband retraction starting at the beginning of retraction (upper left) and going through early dorsal closure (lower right) from a lateral view. Anterior is to the left, posterior is to the right, dorsal is to the top, and ventral is to the bottom. Scale bar represents 20 µm.

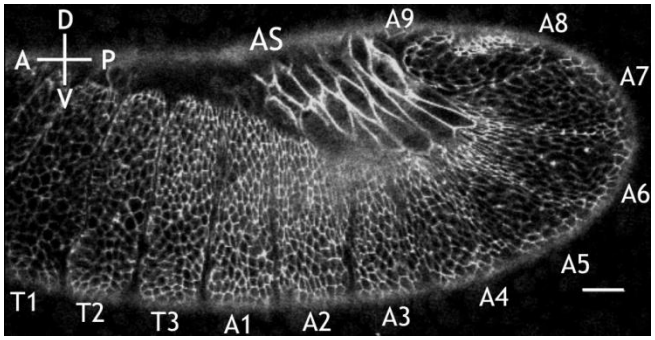

Figure 1.4. Confocal image of mid-to-late germband retraction. Germband segments are each labeled (T1-T3, A1-A9) as is the amnioserosa (AS). Anterior (A) is to the left, posterior (P) is to the right, dorsal (D) is up, and ventral (V) is down, as indicated by the compass in the upper left hand corner. The scale bar represents 20 µm.

The germband is divided into 12 segments: three thoracic segments (T1-T3) and nine abdominal segments (A1-A9) [14] (Figure 1.4). During retraction, furrows form between these segments making their boundaries more obvious. Furrow formation occurs as cells along the boundaries constrict apically, eventually becoming bottle shaped, pulling along their neighboring cells until the grooves between boundaries are 3-4 cell diameters deep [15]. Throughout germband retraction there is no cell division or cell death and very little cellular rearrangement [13,16], thus germband retraction is not driven by intercalation or loss of cells. The amnioserosa and the germband maintain their connections throughout retraction except at the caudal end of the germband (segments A8 and A9). Here the amnioserosa actually overlaps and migrates over the end of the germband [13].

Germband retraction fails in several *Drosophila* mutants. The most severe of these are the u-shaped group mutants, *hindsight*, *serpent*, *u-shaped*, and *tail-up*. At the start of germband retraction, segment A8 is typically over segments T1and T2 (Figure 1.3). Thus the amount of retraction in mutant embryos can be quantified by the location of A8 later in development. Using this marker, *u-shaped* and *serpent* mutants cause the largest disruption to retraction with A8 over segment T3 or A1 for *u-shaped* and over T2 or T3 for *serpent*; *hindsight* and *tail-up* have less disruption with segment A8 over A2 in both [17]. In all of these mutants, the amnioserosa has an abnormal shape during germband retraction. The abnormal shape is apparent before germband elongation in *serpent* mutants, but only at the start of germband retraction for the other three [17]. In all of these mutations, the amnioserosa is not a continuous tissue, due to either premature apoptosis (*serpent*, *hindsight*, and *u-shaped*) or less elongated amnioserosa cells (*tail-up*)

[17]. The lack of a normal amnioserosa in these mutants suggests some role for the amnioserosa in germband retraction. Indeed, in experiments where the amnioserosa was removed via the expression of *ricin*, 95% exhibited an embryonic lethal u-shaped phenotype [18].

Interestingly, germband retraction also fails when an extra mechanical force, pulling towards the posterior of the embryo, is applied during late germband extension [19]. This suggests that germband retraction requires a delicate balance of forces, perhaps originating from the germband or amnioserosa. Previous work has studied the role of both the amnioserosa and germband in retraction [13,16], but has remained inconclusive about the mechanical contributions of each tissue. Lamka and Lipshitz presented evidence that the role of the amnioserosa in germband retraction might be limited to signaling [16]. They worked with one of the u-shaped group, *hindsight* mutants, where the amnioserosa undergoes premature apoptosis and germband retraction fails. Flies in which *hindsight* is blocked can be partially rescued by an overexpression of the *Drosophila* homolog of the insulin receptor even though the amnioserosa still undergoes premature apoptosis. Figure 1.5 shows that although *hindsight* mutants with overexpression of the insulin receptor homolog retract more than mutants without, they still do not fully retract. Since the insulin receptor homolog is only present in germband cells, these results suggest that it is activated downstream of *hindsight*, and that signaling between the amnioserosa and the germband plays a role in germband retraction.

Lamka and Lipshitz then considered what happened in *hindsight* mutant embryos in which premature apoptosis was blocked using embryos that lack three cell death genes [16]. Even in these flies, which retain their amnioserosa, germband retraction was

aberrant, leading them to conclude that the amnioserosa's role in retraction was solely signaling; however, it has not been determined if the mechanical properties of the amnioserosa remain unchanged in *hindsight* mutants. If the mechanical properties are not retained, preventing apoptosis by blocking cell death genes would not be expected to rescue retraction since the mechanics of the amnioserosa would remain aberrant.

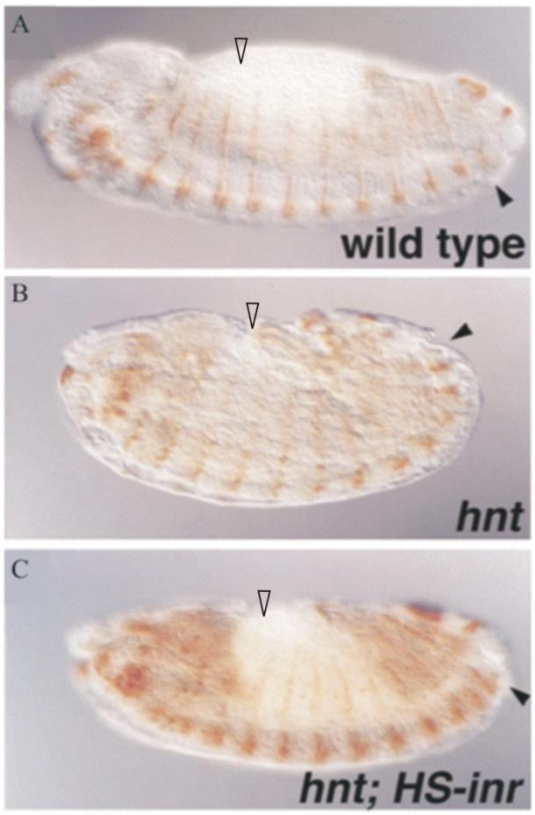

Figure 1.5. Post germband retraction embryos in (*A*) wild type, (*B*) *hindsight* mutant, and (*C*) *hindsight* mutant with an overexpression of the insulin receptor homolog. Solid arrowhead marks segment A8 in each embryo. Open arrowhead indicates approximately where segment A8 would have been located at the beginning of germband retraction. Although the double mutant has retracted more than the *hindsight* mutant, it still has not fully retracted as can be seen by the location of segment A8. Figure modified from [16].

Schöck and Perrimon used observational evidence of cell movements during germband retraction to argue for a more active role for the amnioserosa [13]. They noticed that where plasma membranes of amnioserosa cells attach to the germband, the

cells of the germband are pulled in (Figure 1.6*A*). If one approximates the cells as a foam, with the intercellular tension only along cell edges, then the observed concave border between the germband and amnioserosa suggests that the amnioserosa is pulling on the germband. Under similar assumptions, one would expect a convex border if the germband were instead pushing on the amnioserosa (Figure 1.6*B*). On a cautionary note, the assumption that cells carry most of their tension along their edges remains to be proven. In the following stage of development, it has been shown that cells in the amnioserosa behave more like a continuous sheet, with tension carried by both the cells' apical surfaces and lateral cell-cell interfaces [1].

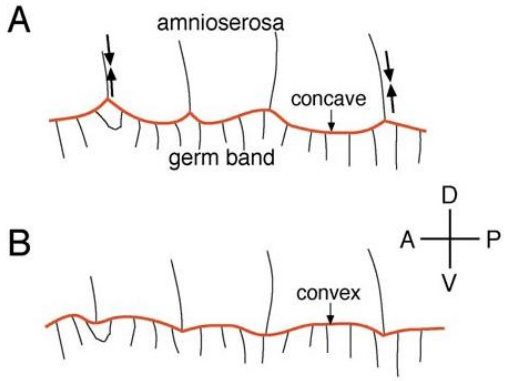

Figure 1.6. Schematic representations of the intersection between the amnioserosa and germband. (*A*) The intersection as actually observed during germband retraction and (*B*) the expected result of a passive amnioserosa and an active germband. This expectation assumes tension is carried along the cell-cell interfaces. Figure reproduced from [13].

Schöck and Perrimon also found that in embryos with mutations in *rho A* expression in the amnioserosa, germband retraction is severely disrupted [13]. *Rho A* is implicated in actomyosin contractility and cell-matrix adhesion. Thus it is more essential for cells actively changing their shape than for those reacting passively. The lack of retraction in these embryos suggests that the cells in the amnioserosa are actively changing shape. Interestingly, *rho A* mutations in the leading edge cells of the germband

do not disrupt retraction, suggesting that they are not actively changing shape, but rather passively reacting to their mechanical environment.

It is possible that structures outside the amnioserosa and germband contribute to germband retraction. The vitelline membrane does not contribute to the basic mechanics of retraction, since embryos shorten their germband normally in its absence [20], despite the embryos' aberrant shape. On the other hand, the yolk may play a role in germband retraction [21]. As germband retraction begins, the amnioserosa and underlying yolk sac have transient contacts originating from both the amnioserosa and yolk. As retraction progresses, these become more persistent, first in the dorsal-anterior region of the amnioserosa and then moving towards the posterior through the rest of retraction. In *myospheroid* mutants, the more persistent contacts between the amnioserosa and yolk are not established. These mutants fail to retract 40-60% of the time [22], indicating that persistent contacts between the yolk and amnioserosa may play a role in germband retraction. Another possible cause for the failure of retraction is the fact that *myospheroid* mutants have no β-PS integrin, which is required for the amnioserosa to overlap the caudal end of the germband [23]. In these mutants, the lamellipodia that usually connect the amnioserosa to the caudal end of the germband are absent.

1.3.1.4 Dorsal closure

Dorsal closure immediately follows germband retraction and lasts from about 10 to 13 hours after fertilization [3]. As closure begins, the amnioserosa covers much of the embryo's dorsal surface in a tear drop shape (Figure 1.7). At this stage, the yolk is directly below the one-cell thick amnioserosa [5]. The adjacent lateral epidermis, called

the germband during retraction, advances from the lateral sides of the embryo to eventually cover the amnioserosa. The engulfed amnioserosa cells then undergo apoptosis [5]. Interestingly, the leading edge of the lateral epidermis actually behaves as a unique tissue, forming an intercellular purse string [5].

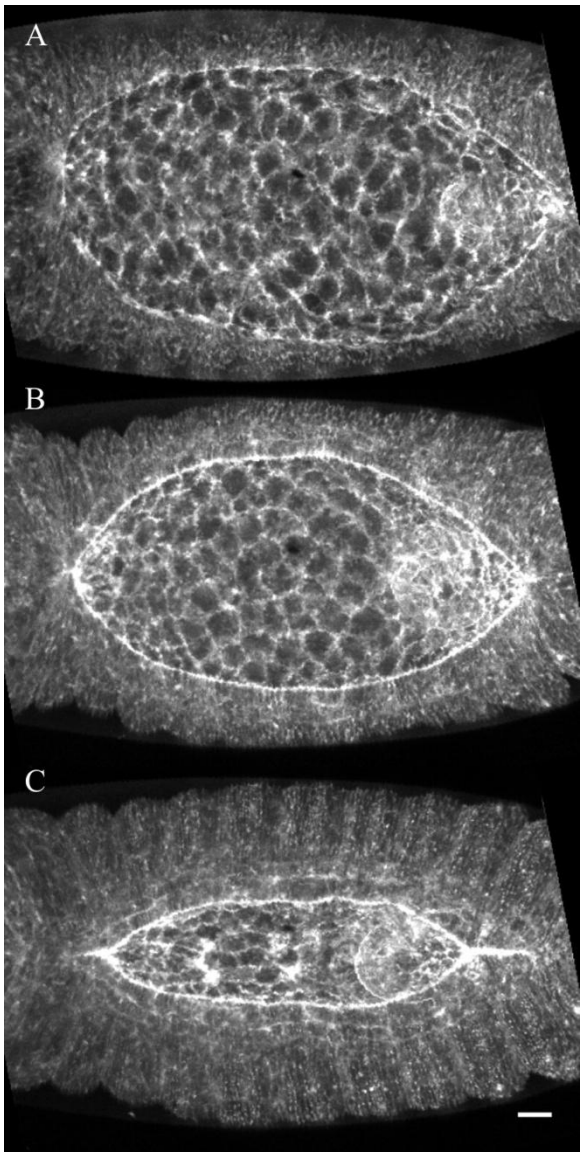

Figure 1.7. Dorsal views of (*A*) early dorsal closure, (*B*) mid dorsal closure (1 hr from *A*), and (*C*) late dorsal closure (2 hrs from *A*). Anterior is to the right. All are projections of z-stacks taken in a sGMCA embryo. Since the stack goes 50 µm deep into the embryo, the hindgut can be seen under the posterior portion of the amnioserosa. Scale bar represents 20 µm.

Both the amnioserosa and the leading edge of the lateral epidermis contribute to dorsal closure, but neither of them is absolutely required. The absence of either alone is insufficient to prevent closure [4,5]. Cells in the amnioserosa undergo pulses of apical constriction to bring the two lateral flanks of epidermis together. The leading edge of the epidermis forms a myosin rich intercellular 'purse-string' similar to those seen in wound healing assays [5]. Wherever the two sides of the epidermis are sufficiently close, filopodia reach across the amnioserosa to make connections with the opposite flank, helping to zip the tissue together [24]. This is especially prominent at the two canthi of the amnioserosa, where the two lateral flanks of epidermis are in close proximity throughout closure. In contrast to the leading edge, the bulk of the lateral epidermis actually opposes closure as the cells are pulled towards the dorsal midline [5].

As dorsal closure proceeds, cells in the amnioserosa deepen and take on a wedge-shaped morphology, typical of tissues that undergo apical constriction. Some cells in the amnioserosa undergo apoptosis during closure, on the order of 13 out of 110, further contributing to a reduction in the surface area covered by amnioserosa cells [5]. The remaining amnioserosa cells apoptose shortly after being covered by the advancing epidermis. Cells in the leading edge actually crawl over one row of amnioserosa cells and maintain contact with them until the amnioserosa cells undergo apoptosis [5].

Figure 1.8 shows a schematic representation of an amnioserosa cell undergoing apical constriction, identifying three possible mechanisms. During dorsal closure amnioserosa cells have an apical actomyosin belt around the apical surface that could constrict and thus cause the apical surface to constrict. In addition to this belt, cells have an actomyosin mesh along their apical surface that could contract to cause apical

constriction. On the other hand, if cell volume is conserved in the cells, expansion of a similar actomyosin mesh along the basal surface would also lead to apical constriction.

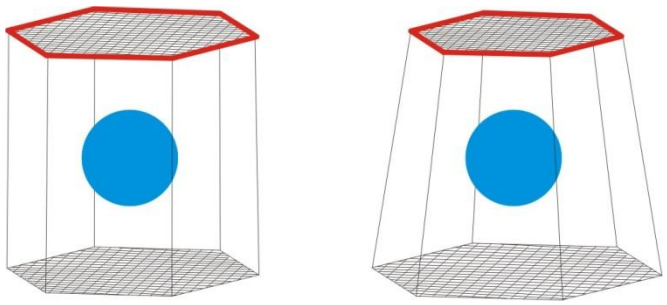

Figure 1.8. Schematic representation of an amnioserosa cell showing its apical actomyosin belt (red), apical and basal actomyosin meshes (meshwork), and nucleus (blue). (Left) Prior to constriction and (Right) after apical constriction and the associated basal expansion. Apical surface is to the top.

1.3.2 The physics

1.3.2.1 Viscoelasticity

To understand the physics of development it is important to understand the physical properties of the cells and tissues involved. Cells have a viscoelastic nature due to the composition of cytoplasm and cytoskeletal filaments. Like other viscoelastic materials, they act neither as a purely elastic solid nor as a viscous liquid, but rather as something in between. To highlight the differences between elastic solids, viscous liquids, and viscoelastic materials, we will consider the reaction of each to a step-like application and removal of an external stress. An elastic solid will deform in response to the applied stress and maintain that deformation until the stress is removed. Once the stress is removed, it will return to its original shape (Figure 1.9*A*). On the other hand, a viscous liquid has a constant flow rate under constant applied stress and will remain at its maximum deformation after stress is removed (Figure 1.9*B*). When a constant stress is

applied to viscoelastic materials, they have periods of time where they act more like an elastic solid and others where they react more like a viscous liquid. Depending on how they recover after a stress is removed, viscoelastic materials can behave more as a liquid or more as a solid. In all viscoelastic materials, some of the deformation will be recovered after the removal of stress, but only in those that behave like a solid will the original shape eventually be recovered (Figure 1.9*C*,*D*). A cell will behave more like a solid as long as its cytoskeleton reacts only elastically and does not reorganize. When the cytoskeleton does reorganize in response to an applied stress, it will not return to its original shape when the force is removed, acting more like a viscous liquid.

The most fundamental physical description of viscoelastic materials has evolved from Boltzmann's 1874 superposition theory, which accounted for memory in strained materials [25]. Viscoelastic materials can be treated as having a memory, since applying a second stress to a viscoelastic material causes a new time response, while the material continues to respond to the first stress. Because of this, the stress and strain responses depend on the strain and stress history of the material, respectively [26].The current fundamental physical description of these materials is given by their relaxation and creep functions [26], which are properties of the material that relate the strain and stress to the stress and strain histories of the material respectively. The formulations for stress, σ, and strain, ε, in viscoelastic materials are

$$\sigma = \int_0^t G(t-\tau)\frac{d\varepsilon(\tau)}{d\tau}d\tau \tag{1.1}$$

and

$$\varepsilon = \int_{-\infty}^t J(t-\tau)\frac{d\sigma(\tau)}{d\tau}d\tau, \tag{1.2}$$

where G is the relaxation function, J is the creep function, and t is the current time.

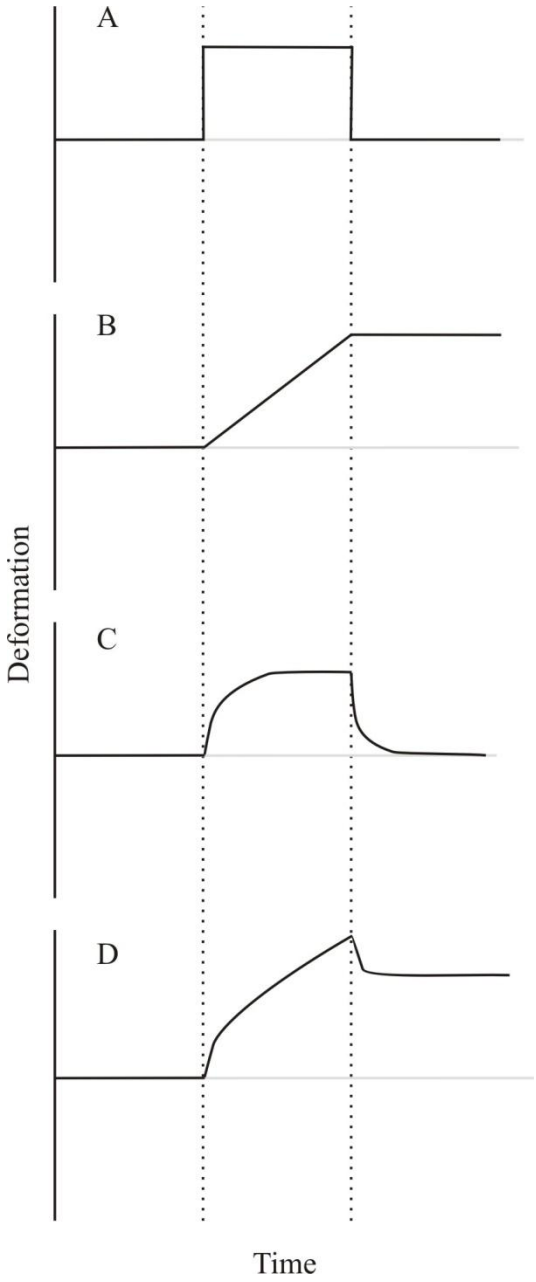

Figure 1.9. Deformation versus time plots for a constant stress applied between dashed lines for (*A*) an elastic solid, (*B*) a viscous liquid, (*C*) a viscoelastic solid, and (*D*) a viscoelastic liquid. Note that the viscoelastic solid still reaches a maximum deformation while the viscoelastic liquid continued to flow. Also note that both viscoelastic materials have some recovery after the removal of the stress.

Using a step application of strain ε_o, equations 1.1 reduces to

$$G(t) = \frac{\sigma(t)}{\varepsilon_0}. \tag{1.3}$$

Similarly, as step application of stress σ_o in equation 1.2 yields

$$J(t) = \frac{\varepsilon(t)}{\sigma_0}. \quad (1.4)$$

Thus, experiments to determine the viscoelastic properties of cells typically measure the creep or relaxation function using an experimental set up that allows for a step change in strain or stress. Many labs are currently trying to measure the properties of embryonic *Drosophila* cells *in vivo*, but the inaccessibility of cells due to the vitelline membrane has made that challenging. The exact properties of these cells remain unknown.

1.3.2.2 Modeling cell mechanics

Although models are often based on an incomplete set of data about the physical properties of cells and the role of genes in cell behavior, they are still used to make predictions about untested cell properties. The model's prediction becomes a new hypothesis that can then be tested to make a better generation of models. For example, experiments typically find a creep function from an applied stress, independent of model [27-29]. The creep function is then fit to a model, typically one that uses mechanically equivalent circuits or a power law. Information about the viscosity and elastic modulus of the cell can then be extracted from the model's parameters.

One of the common ways to model a cell is to use a mechanically equivalent circuit [27,29]. Such models use springs to represent the cell's elastic response and dashpots to represent its viscous response [30]. These elements can be linked together in series or parallel to create different types of viscoelastic models. The springs are idealized to reach a maximum deformation immediately upon an application of force and to return immediately to their initial length upon force removal. Dashpots are idealized to have a

linear deformation rate when a force is applied. Two common viscoelastic elements are the Kelvin-Voigt body and the Maxwell body, drawn schematically in Figure 1.10.

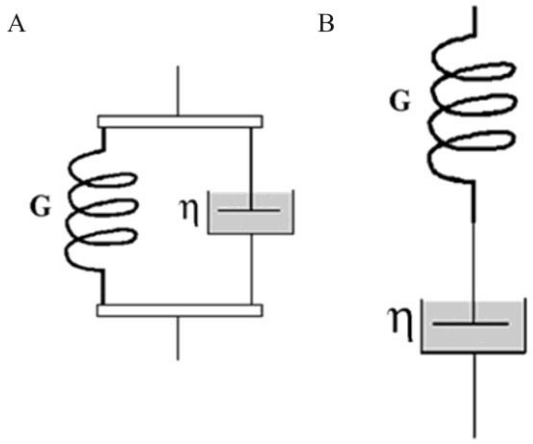

Figure 1.10. Schematic of (*A*) a Kelvin-Voigt body and (*B*) a Maxwell body. G represents the elastic modulus for the spring and η represents the damping coefficient of the dashpot. This figure was reproduced from [30].

The Kelvin-Voigt body consists of a spring and dashpot in parallel [30]. Using a step application of stress, the creep function for this model is given by

$$J(t) = \frac{1}{G}\left(1 - e^{-\frac{\eta}{G}t}\right), \tag{1.5}$$

where G is the elastic modulus for the spring and η is the damping coefficient for the dashpot. Thus in this model, application of a constant force slowly deforms the element, with the initial rate determined by the dashpot. This model eventually reaches a maximum deformation determined by the new equilibrium length of the spring. Thus, its long time behavior is more like a solid than a liquid. Upon the removal of force, this element eventually reaches its original shape via an exponential decay with time constant η/G.

A Maxwell body consists of a spring and a dashpot in series [30]. Using a step application of stress, the creep function for this model is given by

$$J(t) = \frac{1}{G} + \frac{t}{\eta}, \tag{1.6}$$

Upon application of a constant force, the spring will immediately reach its new equilibrium length. The dashpot will then slowly expand like a liquid, making the long term behavior of a Maxwell body more like a viscous liquid. After the force is removed, the spring will immediately return to its original equilibrium length, but the entire element will not return to its original shape.

More complicated models can be built using the same basic elements used to construct the Kelvin-Voigt and Maxwell bodies. Creep functions with more than two phases can only be modeled by adding elements. Of course, the more complicated the element, the more parameters in the model. Figure 1.11 shows a three-phase creep function and the mechanical equivalent circuit used to model it. The three phases of the creep response curve are an elastic phase, a relaxation phase, and a viscous flow phase. They modeled this behavior using a dashpot in series with a standard linear solid model (a Maxwell body in parallel with an additional spring). The first phase is dominated by the deformation of both springs (k_0 and k_1). The second phase allows these springs to reach equilibrium with a time constant determined by the viscosity of dashpot γ_1. The third phase is the continuing expansion of dashpot γ_0.

An alternative way to model the creep function is with a power law. A typical form for the creep function *J* in such a model is given by

$$J(t) = Dt^{\alpha}\ , \tag{1.5}$$

where *D* and α are the parameters used to fit the data. This is the sort of behavior that occurs during sol-gel transitions in soft glassy materials [31]. In essence, power law

behavior suggests that the creep function is not described by a few distinct relaxation times. Instead, relaxations from all time scales are present simultaneously [31].

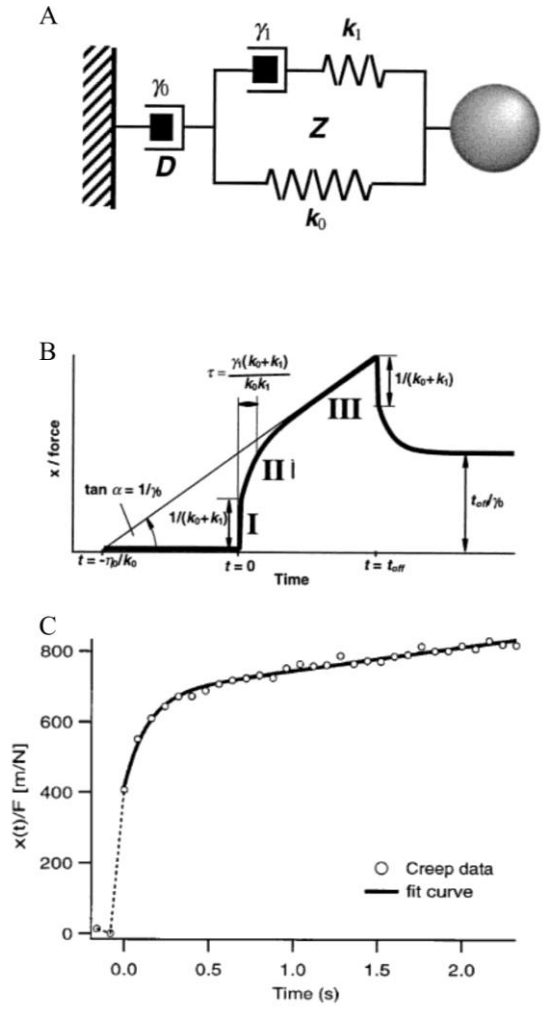

Figure 1.11. (*A*) The mechanical equivalent circuit used by Bausch *et al* to model their experimental data. (*B*) The creep function for the mechanical equivalent circuit shown in *A*. Notice that it has three phases: in the first, the springs instantaneously expand, a purely elastic response; in the second, spring k_0 controls the total amount of deformation, but its rate is determined by dashpot γ_1; and in the third, only dashpot γ_0 continues to expand, a purely viscous flow. (*C*) The creep data from their experiment along with its fit using this mechanical equivalent circuit. This figure was reproduced from [27].

Lenormand *et al*. tested the responses of three different cell types under various conditions and compared their measured displacements over three time decades with the displacements expected from both a mechanical equivalent circuit and a power law [31]. They used a mechanical equivalent circuit that consisted of a Kelvin-Voigt element in

series with a Maxwell element. They found that both this circuit element and the power law had good agreement with the data over at least one time decade, but that the power law was a better fit over all time decades. They could have added enough parameters and elements to make a mechanical equivalent circuit work, but it is unclear that such a model would have any real physical meaning.

1.4 Materials and Methods

1.4.1 Confocal microscopy

Images were captured using a Zeiss LSM410 laser-scanning confocal microscope (inverted) with a 40×, 1.3 NA oil-immersion objective and 488-nm excitation at typical scanning times of 8 s per frame (Figure 1.12). Laser-scanning confocal microscopy was developed in the 1980s by putting together two separate developments from the 1950s: confocal microscropy and flying-spot microscopy (later called laser scanning) [32]. Before getting into the details of these two types of microscopy and how they combine, I will first briefly outline conventional fluorescent microscopy.

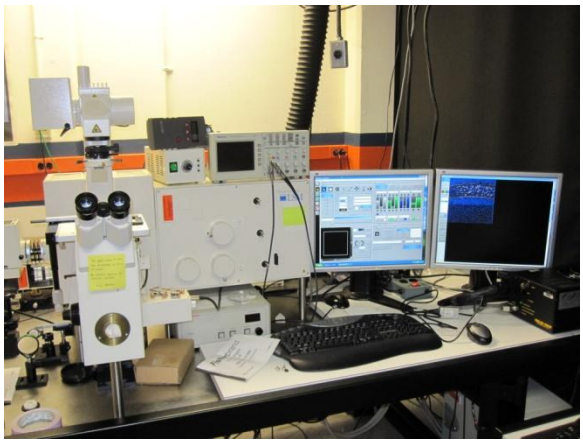

Figure 1.12. Our Zeiss LSM410 laser-scanning confocal microscope.

In fluorescent microscopy, a fluorescent sample is exposed to light at an excitation wavelength, in our system using a laser. The excitation and emission wavelengths will depend on the fluorescent molecules present. In the data presented here, we used green fluorescent protein (GFP) to label our samples. GFP is a small, naturally fluorescent molecule with good resistance to photobleaching [33]. Its gene can be fused with the gene for a protein of interest. This transgene is then inserted into the fly genome, so that subsequent generations express a green fluorescent version of the protein of interest. More details can be found below under fly strains.

In our system, fluorescent samples are excited with the 488-nm output of an air cooled krypton argon laser. GFP emission is broad, peaking at 508 nm, but extending from around 475 nm to over 600 nm [34]. This emmision can be separated from the excitation wavelength using color filters, allowing just the emitted light to be collected. In conventional microscopy, light emitted from every plane of the sample reaches the detector. This obscures fine features in thick, auto-fluorescent samples like a *Drosophila* embryo.

To circumvent this problem, confocal microscopy uses a pair of pinholes to greatly reduce the amount of out-of-focus light that reaches the detector. This increases its resolution along the optical axis and allows for optical sectioning, *i.e*., collection of 3D images even in live samples. The name confocal is used because the two pinholes and the imaged plane in the sample are all *con*jugate *focal* planes [35] (Figure 1.13). The pinholes can be adjusted to allow more light to reach the detector at the price of a loss in resolution.

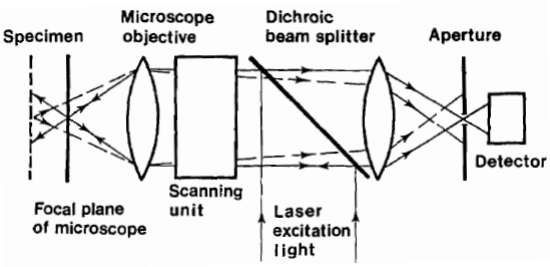

Figure 1.13. Schematic of the beam path in a scanning confocal microscope. Pinhole (marked aperture) keeps out of focus light from hitting the detector. Specimen extends from the focal plane to the left. Light emitted from the specimen at the focal plane is focused by the optics through the pinhole (solid line). Light emitted from the specimen, but outside the focal plane is not focused at the aperture and thus does not reach the detector (dashed line). A second pinhole is in front of the illumination laser, and not shown in this schematic. Figure is reproduced from [36].

Since confocal microscopes measure fluorescence from only one point at a time, they require a method of building up collected points throughout a sample. In early implementations, this was done by moving the sample [32], but this proved inconvenient due to slow scan times. Another type of microscopy was developed in the early 1950s that did not limit out of focus light, but did build an image from individual points in an effort to increase focal plane resolution. This method, originally called flying-spot microscopy, but now called laser scanning microscopy, creates a point of light that is raster scanned across a sample to build up a higher contrast image [37]. When the excitation beam is raster scanned across a sample, frame times below 1 frame/s can be achieved in confocal systems, albeit with decreased image quality for shorter exposure times. Even though laser scanning microscopes raster the beam across the x-y plane, the objective or sample stage must be moved to collect multiple frames along the z-axis. This is done precisely under computer control using a fine z-motor and can be repeated through time with set pause intervals.

1.4.2 Fly strains

We used two strains of *Drosophila melanogaster*: ubi-DE-CAD-GFP (Drosophila Genetic Reseach Center, Kyoto, Japan) [38] and sGMCA (gift from DP Kiehart) [5]. Both of these fly strains tag a native protein with green fluorescent protein (GFP). GFP originates from the jellyfish *Aequorea victoria* [39]. This protein was cloned and modified for improved use as a fluorescent marker in living tissue. The emission peak for GFP variants is around 508 nm. The original GFP had double excitation peaks at 396 and 475 nm [40], but many of the improved variants have single excitation peaks near 488 nm, which is one of the standard wavelengths for excitation in older laser scanning confocal microscopes.

Our primary strain is ubi-DE-CAD-GFP, in which *Drosophila* E-cadherin (DE-cadherin) is tagged with a green fluorescent protein and ubiquitously expressed [38]. As mentioned above, cadherins are cell adhesion molecules. DE-cadherin localizes to the adherens junctions between cells in *Drosophila* embryos. These junctions are located on cell-cell interfaces close to cells' apical surfaces. GFP-cadherin thus yields good cell edge definition for the apical-most part of cells. Although, only 50% of eggs laid from these flies are fertilized, the fertilized eggs develop normally and are typically considered wild-type [38].

Where noted, we used the sGMCA fly strain. This is a line of transgenic flies in which a modified GFP is fused to the autonomously folding actin binding region of fly moesin. This fusion is ubiquitously expressed using a promoter/enhancer from the *spaghetti squash* gene [5]. It thus labels filamentous actin throughout the embryo. It gives a good view of the cell edges in middle planes of the cell, and shows the actomyosin

meshwork on both the apical and basal surfaces of amnioserosa cells. This strain has normal fly development and behavior, as well as a significantly higher fertility rate than the ubi-DE-CAD-GFP [5]. Unfortunately, the line is not as robust as purely wild-type stocks.

1.4.3 Sample preparation

Embryos are collected for 2 hours on grooved grape-juice agar plates with a small dab of yeast to attract flies (Figure 1.14*A*-*B*). After embryos are collected, they are placed in an incubator for 17-24 hours depending on the stage desired and the temperature of the incubator. The incubator is typically kept between 15°C and 17°C, depending on the timing needs of all members of the lab. In some cases to increase the amount of imaging that can be done in a day, a sample is kept at 4°C after incubation to halt development for a few hours until those embryos can be imaged. No differences were detected in these embryos.

After embryos are incubated to the applicable stage, they are washed off the agar plates and onto a fine mesh (Figure 1.14*C*). This mesh with the embryos is transferred to the side of a funnel clamped to a piece of Whatman paper on a glass filtration stopper, all on top of a Büchner flask (Figure 1.14*D*). The embryos are then washed off the mesh using DI water. The water can be removed from the funnel by turning on the vacuum. Once all of the embryos are off the mesh, they are covered in a bleach solution (50% bleach/50% DI water) for 1.25 minutes. This chemically removes the chorion, making the embryos optically transparent. Embryos are then rinsed in water three times to remove any residue of bleach.

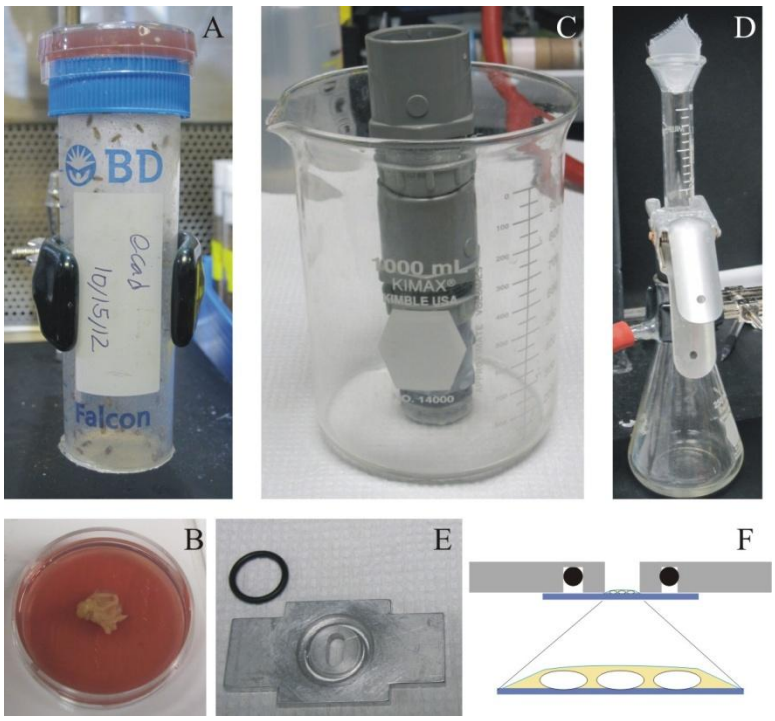

Figure 1.14. (A) Collection vial of *Drosophila* with a wire mesh at the bottom to let in air and a grape-juice agar plate with yeast at the top to attract flies. (B) Grooved grape-agar plate with a dab of yeast for collecting. (C) Set-up for washing the fly embryos off the agar plate. The top gray piece has a large mesh that will catch chunks of agar, but allows fly embryos through; the middle layer has a thin mesh that will catch fly embryos, and the bottom layer keeps the thin mesh above the waterline during washing. (D) The thin mesh ready to be washed of fly embryos into a funnel on top of a Büchner flask. This funnel and flask will also be used for dechorionating the embryos. (E) The metal slide used as a sample holder. The oxygen permeable membrane is placed on the inner circle and clamped down with the O-ring. Vacuum grease is then spread on top of the membrane, but only where the membrane is on top of metal. The oil is dropped into the well the vacuum grease makes and then the coverslip with the embryos is placed on top so the embryos are sandwiched in oil between the coverslip and the oxygen permeable membrane. The coverslip is then secured with nail polish. (F) Schematic of side view of a finished slide, inverted and ready for imaging.

The Whatman paper is then removed from the set-up with the embryos on top. It is very carefully pressed against another agar plate, depositing the embryos onto the plate. Any embryos not transferred by this method can be transferred using a toothpick. The agar plate is then placed under a dissecting microscope where the embryos can be arranged and oriented using a sharpened toothpick. We typically arrange about 30 embryos for a given slide, usually into 3 easy to navigate lines of 10. These numbers may

change according to the number of available embryos and the type of experiment planned.

Once the embryos are lined up, they are transferred to a coverslip by gently pressing on them with a coverslip coated with embryo glue. Embryo glue is the residue from a piece of double-sided tape dissolved in heptane. As the heptane evaporates, it deposits a thin sticky layer onto the coverslip. The coverslip is often rolled against the agar to prevent smashing the embryos. In such cases, one must compensate for the rolling-induced change in orientation during initial alignment. Slight modifications to the embryo's orientation can be made using a toothpick after transfer to the coverslip, but the coverslip is much less forgiving than the agar; without extreme care, the embryo is often destroyed. For lateral images in germband retraction, the coverslip with the embryos is set aside for 3-5 minutes, allowing some dehydration of the embryos which causes a slight flattening. This allows more of the normally curved lateral surface to be seen in one confocal plane.

Once the embryos are transferred to the coverslip, and dehydrated if necessary, they are put on one of two different types of slides. Either they are covered in halocarbon 700 oil (Sigma-Aldrich, St Louis, MO) and are then immediately ready for imaging (mostly used in experiments where the goal was to look at the other side of the embryo after a damaging series of ablations to one lateral side), or they were mounted on a metal slide (Figure 1.14*E*, *F*) in a thin layer of halocarbon 27 oil (Sigma-Aldrich, St Louis, MO) between the coverslip and an oxygen-permeable membrane (YSI, Yellow Spring, OH). This membrane is separated from the coverslip by a thin layer of vacuum grease and attached to the metal slide via an O-ring.

For experiments designed to image and ablate on opposite sides of the embryos, the embryos are lined up as close as possible to the edge of the coverslip. After imaging and ablating one side, a small piece of parafilm is added to the slide to act as a spacer. This protects the embryos as a second coverslip is then placed on top of the embryos and parafilm. The sample is then flipped so that imaging takes place through the second coverslip. Unfortunately even when the embryos were within 500 μm of the edge of the coverslip, embryos in the double coverslip setup do not get enough air for normal development. Thus, long time sequences of the second side of an embryo are not possible.

1.4.4 Laser microsurgery

Laser microsurgery can be a useful technique for perturbing part of a biological system in a known way and using the results to draw conclusions about the mechanics of the unperturbed process. Pulsed lasers can create localized perturbations with sub-micron precision [41], allowing for the precise destruction of a cell, group of cells, or even sub-cellular features [42].

Our laser microsurgery system ablates using the third harmonic (355 nm) of a Q-switched Nd:YAG laser (5 ns pulsewidth, Continuum Minilite II, Santa Clara, CA). This laser is coupled into our imaging microscope with independent beam steering for the ablation laser via a computer-controlled steering mirror. This setup allows simultaneous ablation and imaging. Computer-control of the steering mirror is through a custom plug-in for ImageJ (NIH, Bethesda, MD). This plug-in allows a user to draw any shape on a recently acquired image and then moves the steering mirror at a user-defined velocity to

reproduce that shape with the ablation laser. Since the ablation laser is pulsed, the rate at which the steering mirror moves determines the spacing between individual ablation points. To create a smooth cut with a 10 Hz repetition rate requires slow steering rates (5-10 μm/s).

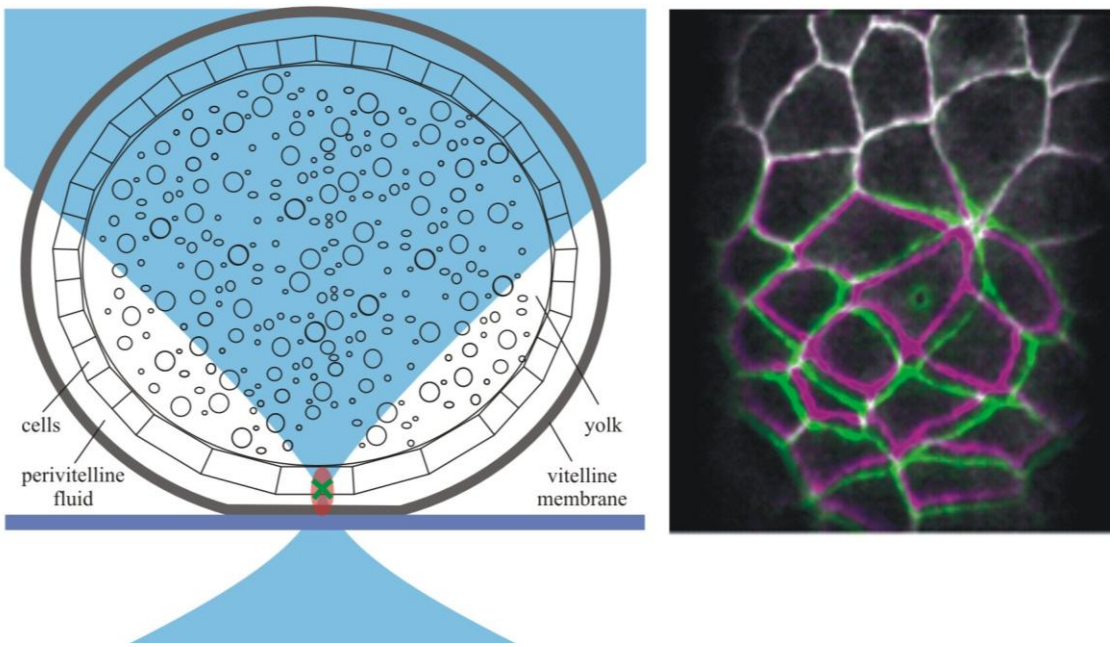

Figure 1.15. (Left) Cross-sectional sketch of an embryo during ablation. The focused laser (blue) ablates through the vitelline membrane, the perivitelline fluid, and the cell, but does not ablate the yolk underneath. The red ellipse represents the ablated region and the green 'x' where the laser was focused. (Right) Image of a cell sheet post-ablation (green), with the pre-ablation cell location overlayed (magenta). Hyper-fluorescent ring (green) indicates ablation point and is caused by ablating the vitelline membrane.

The pulse energy of the ablation laser is controlled using two polarizers. The first is crossed with respect to the second to smoothly vary the fraction of light transmitted. The second remains at a fixed polarization so that changes in energy do not affect the polarization of light through the rest of the beam path. Pulse energies are measured via a pick-off mirror that directs a small percentage of the beam to an energy meter. The amount of energy at the pick-off detector is periodically calibrated with the amount of energy reaching the sample. The pulse energy chosen is sufficient to cut through the

vitelline membrane, paravitelline fluid, and the cell without puncturing the yolk sac underneath (Figure 1.15).

1.4.5 Segmentation and cell tracking

For even a handful of cells in a time-lapse image set, cell segmentation is a time consuming process. Thus researchers have developed many automated systems for image segmentation. Unfortunately, images often have artifacts that lead to segmentation errors with these automatic routines, *e.g.*, bright pixels in the center of a cell. In such cases, one can use semi-automated segmentation routines that allow the user to inspect each frame and correct the automated software's misjudged boundaries using a range of tools. Such routines increase the speed of segmentation (compared to manual methods) without a large loss in accuracy. We used software products that allow user intervention in an otherwise automated watershed algorithm to segment germband cells. We originally used PackingAnalyzer [43] to segment cells, but did not use its cell tracking features. We later switched to segmenting and tracking cells using SeedWater Segmenter [44], a software tool developed in our lab.

SeedWater Segmenter uses a watershed algorithm that requires an initial set of starting pixels or seeds. For best results, these are placed in the darkest region of each cell. Each seed is associated with one segmented region, but each region can have multiple seeds. The watershed algorithm builds out from each seed until it meets another region, eventually assigning all pixels to some region. In SeedWater Segmenter, the original seeds are chosen using a Gaussian blur, but these can be modified by the user until they correctly identify cells. Since we usually concentrated on segmenting only a

portion of the cells in an image, the Gaussian range was typically chosen to yield almost no seeds. The rest were added manually. Seeds for subsequent frames are calculated from the centroids of segmented cells in the preceding frame. Occasionally, the cells would move too far between frames for this to be accurate, but this was easily remedied using SeedWater Segmenter's tools for moving a seed or group of seeds.

Most of the user manipulations in SeedWater Segmenter involve the addition of extra seeds. Most additional seeds are added to fill regions of a cell that are misassigned. These can even be drawn as a line to define a particularly troublesome boundary. Seeds can be saved and reloaded for additional editing at a later point. Extra seeds are not propagated to the next frame during normal use, but that can be overridden if desired. Cell values can also be reassigned to fix any tracking errors.

1.4.6 Finite-element model

Modeling of both line incisions in germband segments and laser-hole drilling in the amnioserosa was undertaken using custom-written, cell-level, 2D finite-element models (software supplied by G.W. Brodland, U.Waterloo, Ontario, Canada) [45,46]. In essence, problems solved using the finite-element method break a complicated system into a series of differential equations, which are then numerically solved in small steps. Typically, in order to implement a finite-element model, the region to be modeled is divided into a fine mesh, and analysis is done on the nodes of the mesh. In our case, the finite-element model solves for the incremental displacement of each node in each step. By integrating multiple steps, the model can reproduce the movement of cells in a tissue in response to a wound.

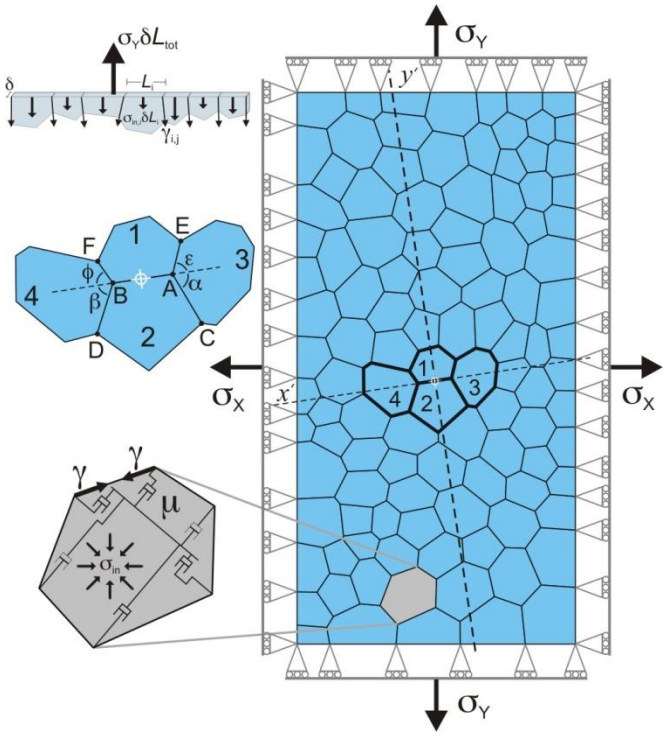

Figure 1.16. Cell-level finite-element representation of an epithelium: (*upper inset*) force balance along one edge of a cell patch; (*middle*) the local wound geometry; and (*lower*) the model for each cell. Reproduced from [6].

As shown in Figure 1.16, an epithelium is modeled as a two-dimensional patch of tightly packed cells. Care was taken to match the cell size and density between the simulated patches and the experimental cell patches. This was done by matching the spatial scale factor ρ, where

$$\rho = \frac{total\ edge\ length}{total\ cell\ area}\ [47]. \tag{1.6}$$

Each cell in the epithelium is a polygon with edges that represent cell-cell interfaces and nodes at cellular triple junctions (Figure 1.16). Although junctions with more than three cells occur frequently in living tissue, they are typically avoided in simulations. During development cells can rearrange by basically eliminating an edge between one pair of cells and forming an edge between another set of cells in a process called a neighbor exchange. These exchanges involve junctions between at least four cells and cause errors

in the simulation. To solve this problem, junctions with more than three cells are avoided in simulations using the method shown in Figure 1.17. Edges that reach a minimum length flip connectivity. In our simulations, neighbor exchange was typically not allowed.

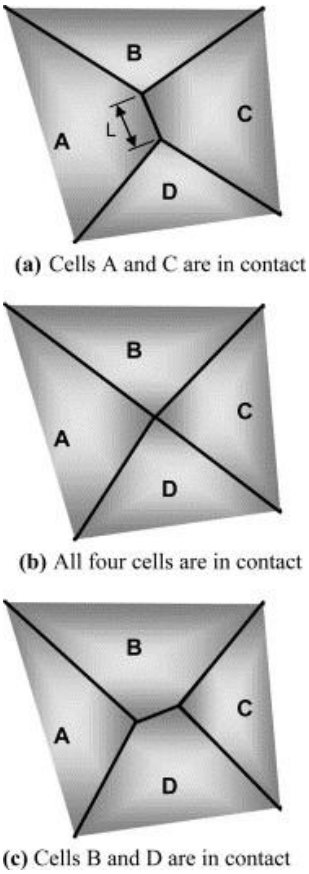

Figure 1.17. Cell rearrangement. (*a*) Prior to rearrangement, cells A and C are in contact. (*b*) As the edge between cells A and C shrinks to zero, all four cells are in contact. (*c*) As cells A and C move apart, a boundary forms between cells B and D. In the finite-element model that allows neighbor exchanges, once the length L of the edge between cells A and C reaches a minimum value, the model will switch to the configuration shown in (*c*) with the new cell edge between B and D just over the minimum value. Reproduced from [48].

In the base finite-element model, each cell has three mechanical contributors: each cell-cell interface has a tension, γ, representing both contraction of circumferential microfilament bundles and a tangential equivalent for cell-cell adhesion [49]; each cell has a system of internal dashpots sized to model a uniform equivalent viscosity, μ [45], which represents the deformability of cytoplasm and its embedded cytoskeletal networks;

and each cell is subject to an area constraint, encompassing both pressure from the incompressibility of cytoplasm and in-plane apical/basal tensions from the cortical cytoskeleton [50]. Although interfacial tensions are constant and uniform in the base model, polarization similar to planar cell polarity can be introduced by varying the interfacial tensions with edge orientation. This polarization of edge tension promotes oriented autonomous cell elongation along a globally defined polarization axis by assigning an orientation-dependent cell edge tension

$$\gamma(\theta) = \gamma\left(1 + \frac{f}{2} - f\cos^2\theta\right), \tag{1.7}$$

where f is the polarization factor and θ is the angle between the cell edge and the globally defined polarization axis. With this definition of edge tension, the cells will tend to elongate along the global polarization axis (Figure 1.18).

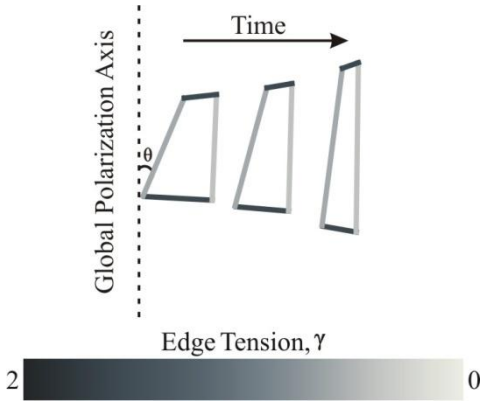

Figure 1.18. Schematic representation of polarization. The globally defined polarization axis runs vertically. Edge tension varies with angle from the polarization axis so that edges close to vertical have low edge tension, while edges close to horizontal have a high edge tension. Through time this will tend to elongate the cell.

Although this base model exhibits system-level viscoelastic behavior [47,51], the full recoil kinematics are only reproduced by adding explicit viscoelastic rods – either along cell edges (germband segment models) or as a pre-stressed intracellular mesh

(double-wound laser hole-drilling models) (Figure 1.19). These rods are necessary because the experiments involve very high strain rates, 1-5 s^{-1}. Previous uses of the base model focused on normal morphogenetic movements in which strain rates are < 0.5 h^{-1} [48,52]. Rod elements are typically a Kelvin-Voigt body in parallel with a Maxwell body, but simpler mechanical equivalent circuits can be used by setting a viscosity or spring constant to zero. For line cuts in germband segments, the model best fit the experimental recoils using just a Kelvin-Voigt body for the viscoelastic rods along cell-cell interfaces.

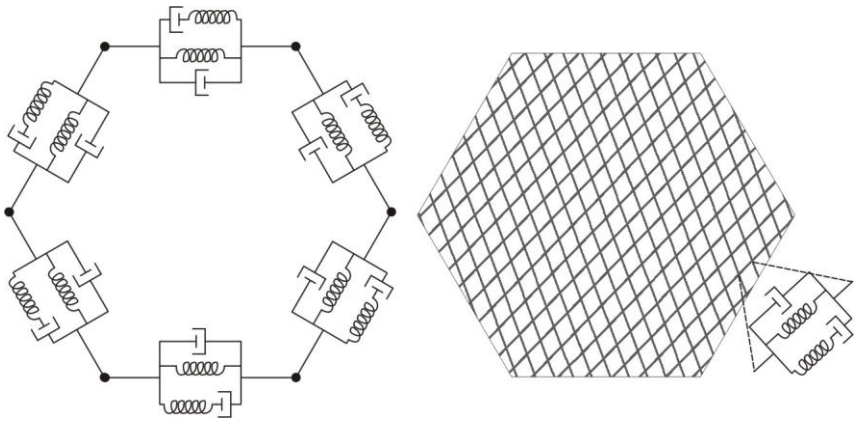

Figure 1.19. Schematic representation of viscoelastic rod elements. Left panel: along cell edges. The springs and dashpots show the viscoelastic rod elements added to each cell edge. These elements act in parallel to cell edge tensions. Right panel: an example of the viscoelastic rod elements as an intracellular mesh.

A simulated epithelium also requires appropriate boundary conditions including constraints that maintain patch shape and constant external stresses σ_x and σ_y that are applied via external forces (Figure 1.16). These forces represent the far-field stress in the embryo, *i.e.*, the forces on the patch from outside the patch. To reproduce recoils from laser hole-drilling experiments, we found that these external stresses need to be ~3× the value that just balances the patch's edge tensions. We thus use triple the balancing stress in our models for the germband segments. We introduce anisotropy in external stress by

varying the far-field stress in each direction so the average external stress $\bar{\sigma}$ constant. Thus, σ_x and σ_y take the form

$$\sigma_y = \bar{\sigma} + \Delta \text{ and } \sigma_x = \bar{\sigma} - \Delta\,, \tag{1.8}$$

and the degree of anisotropy is defined as

$$\frac{\Delta}{\bar{\sigma}} = \frac{\sigma_y - \sigma_x}{\sigma_y + \sigma_x}. \tag{1.9}$$

Computationally, the dynamic behavior of the model is described by [46]

$$(1/\Delta t)\mathbf{C} \cdot \Delta\mathbf{u} = \mathbf{f}, \tag{1.10}$$

which assumes low Reynolds number conditions. In this equation, Δt is a time step, **C** is the damping matrix, $\Delta\mathbf{u}$ is a vector of incremental node displacements, and **f** is a vector that represents the non-viscous forces acting on each node. **C** and **f** are calculated from the current cellular geometry. This system of equations is augmented by applicable constraints using Lagrange multipliers (including "pressures" for the cell area constraints).

The augmented system of equations is solved at each time step to yield values for the Lagrange multipliers and incremental displacements $\Delta\mathbf{u}$. The node positions are updated and the process repeated, allowing the potential accumulation of large deformations. Occasionally due to the numerical nature of the solutions, a cell will have a small change in area despite the area constraint. In this case the simulation is programmed to change the area constraint for that cell so it returns to its original area within a user determined number of steps. Typically this was set to 5 time steps.

CHAPTER 2

GERMBAND RETRACTION: MECHANICAL INTERACTIONS BETWEEN SURFACE EPITHELIA

2.1 Abstract

Germband retraction involves a dramatic rearrangement of the tissues on the surface of the *Drosophila* embryo. As germband retraction commences, one tissue, the germband, wraps around another, the amnioserosa. Through retraction the two tissues move cohesively as the highly elongated cells of the amnioserosa contract and the germband moves so it is only on one side of the embryo. To understand the mechanical drivers of this process, we designed a series of laser ablations in both the germband and the amnioserosa. We found evidence for autonomous furrow formation in the germband and autonomous cell elongation in some of its segments; however, neither is sufficient for germband retraction. They must be assisted by contraction of amnioserosa cells.

2.2 Introduction

Germband retraction is a dynamic stage of *Drosophila* development, but also one where the mechanics are largely unknown. The cell and tissue movements have been well described [13,53]. On the surface of the embryo, two epithelia, the germband and the amnioserosa, move dramatically in concert. At the beginning of retraction, the germband covers most of the dorsal and ventral surfaces of the embryo, curling around its posterior end. Other than a thin bridge over the dorsal surface, the amnioserosa is constrained to

the two lateral surfaces of the embryo (Figures 1.3 and 2.2*A*). As retraction proceeds, the two tissues move together as the germband unfolds and the amnioserosa moves dorsally. By the end of retraction the amnioserosa will inhabit a teardrop shape on the dorsal surface of the embryo surrounded by the germband [13,53]. As the tissues move, their cell shape changes are complementary. The cells in the amnioserosa shorten their long axis, as the cells in the germband elongate towards the amnioserosa, especially those in the rows closest to it [13]. As germband retraction progresses, the boundaries between its 12 segments (T1-T3 and A1-A9) [14] become more distinct as furrows form between them [13,53] (Figures 1.3 and 2.2*A*, *B*).

Our goal is to understand the mechanical interactions that lead to the tissue motions and their accompanying cell shape changes. In particular, does one tissue contribute mechanically to the other tissue's motion? To investigate this, we tested two extreme hypotheses. In the first, the amnioserosa plays an active and dominant mechanical role driving the motion of both tissues i.e., the germband reshapes passively. In the second, cell shape changes in the germband are mechanically autonomous. Our results suggest that the mechanical interactions between these two tissues are far more complicated. Many of the cell shape changes in the germband are mechanically autonomous, but complete unfurling of the germband clearly requires a mechanical assist from the amnioserosa.

Previous work has shown the importance of the amnioserosa for germband retraction [13,16,17,54], but its exact role has not been clear. In a set of mutations where the amnioserosa undergoes premature apoptosis, *u-shaped*, *serpent*, *hindsight*, and *tail-up*, germband retraction fails [17]. This suggests a role for the amnioserosa in retraction,

but *hindsight* mutants can be rescued to an almost wild-type morphology by overexpressing the *Drosophila* homolog of insulin receptor, which is not expressed in the amnioserosa [16], suggesting the amnioserosa's role is at least partially as a source of biochemical signals. In contrast, other research has pointed to a more mechanical role for the amnioserosa. It has been found to actively migrate over the caudal end of the germband [13] and germband retraction is disrupted by mutations that affect cell migration and actomyosin contractility in the amnioserosa. There is no disruption for the same mutations in leading cells of the germband [13].

Laser microsurgery has previously been used to delineate the mechanical contributions of tissues to their motions during development [4,5,55,56]. Here we use laser microsurgery to probe the mechanical role of the amnioserosa and the germband during retraction. The advantage of laser microsurgery is its spatial and temporal control. By investigating individual segments of the germband, we determined that segments around the curve of the germband behave in a way that is distinct from the rest of the tissue. Using laser microsurgery we were also able to design incisions in the amnioserosa that separate its biochemical and mechanical contributions to retraction.

2.3 Experimental Methods

2.3.1 Fly strains

The primary *Drosophila melanogaster* strain used is ubi-DE-CAD-GFP [38] (Drosophila Genetic Reseach Center, Kyoto, Japan), which ubiquitously expresses GFP-

E-cadherin, labeling epithelial cell junctions. Where noted, we used the strain sGMCA [5] (gift from DP Kiehart) to label actin filaments.

2.3.2 Slide preparation and microscopy

Slides are made of 20-30 embryos from two-hour collections. After collection, embryos are kept at approximately 15°C until reaching germband retraction. Some embryos are used directly after this incubation period, others are stored for a few hours at 4°C, halting development, and warmed during slide preparation back to room temperature. No differences were detected. Embryos are dechorinated in a 50% bleach solution, arranged on their lateral side and mounted to a cover slip using embryo glue. The embryos are left uncovered on the slide for approximately 3 minutes before being covered in halocarbon 27 oil (Sigma-Aldrich, St Louis, MO). This exposure leads to a slight dehydration that enables flattening of the embryo, allowing more complete lateral images on a confocal system without using multiple-depth slices. The embryos are finally mounted on a metal slide between the cover glass and an oxygen permeable membrane (YSI, Yellow Spring, OH). Images were captured using a Zeiss LSM410 laser-scanning confocal microscope (inverted) with a 40×, 1.3 NA oil-immersion objective. The scanning time was 8 s per frame.

2.3.3 Laser microsurgery system

Our confocal microscope is coupled with a Q-switched Nd: YAG laser (5-ns pulsewidth, Continuum Minilite II, Santa Clara, CA) used at its 3rd harmonic (355 nm) for ablations. The ablating laser beam is controlled through a steering mirror that can be

driven by computer using a custom plug-in for ImageJ (NIH, Bethesda, MD). This plug-in allows us to draw various shapes on a recently obtained image and have the ablating laser follow the path. The spacing between pulses along this path can be controlled by changing the speed at which the mirror moves. Achieving smooth cuts with a 10 Hz repetition rate requires slow scanning speeds, ~2 s for a 15-µm line.

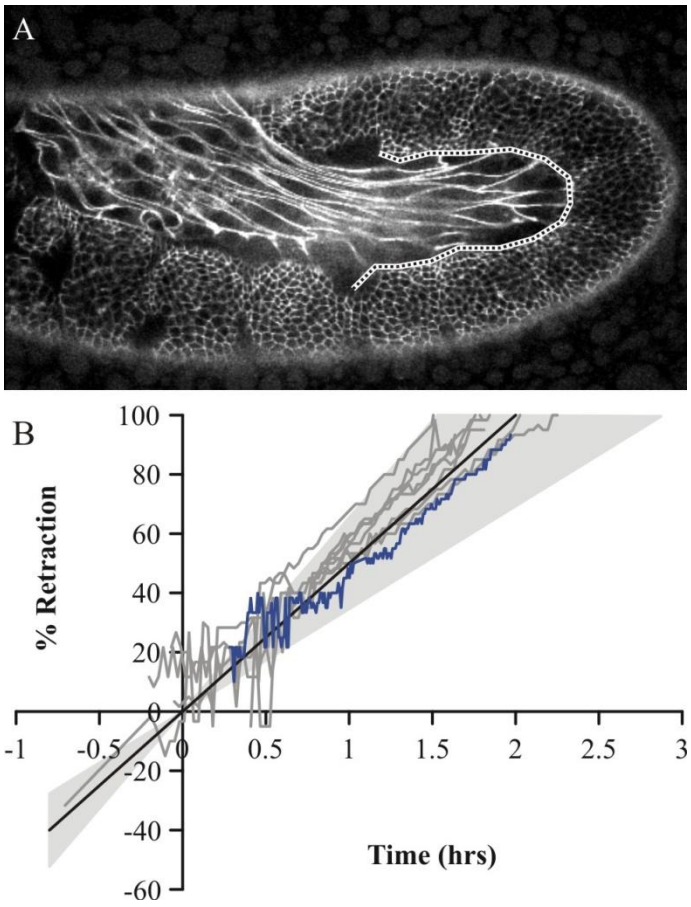

Figure 2.1. Contour staging method. (*A*) lateral view of germband retraction with the staging contour traced with a black dashed line surrounded by white. (*B*) An example of the staging method at work. The solid black line is the average time course of retraction for the standard set (with the shaded gray region covering ±2σ). The gray lines are time courses for individual embryos in the standard set. The blue line is the time course staging of an unablated embryo not included in the standard set.

2.3.4 Image staging

Since our images are taken laterally, we are unable to use a conventional staging method because we could not clearly see the position of the caudal end of the germband as a function of egg length. We thus developed an alternative way to stage our images. We first traced a contour along the amnioserosa-germband boundary from the T3/A1 segment border to that between segments A7/A8 (Figure 2.1*A*). We then matched this contour to a standard set of similar contours constructed from traces of eight unablated embryos. The matching process allows for arbitrary rotations, translations, and uniform scaling. Using a method for contour staging outlined in [57], we simplified our contour matching problem to a linear least squares problem and used a χ^2 test to determine the best matches between contours. Figure 2.1*B* shows a time-lapse set of contours from one unablated embryo staged against the standard set. For wounded embryos, where the contours are not exact matches for any member of the standard set, our staging method assigns a staging range based on all of the contours that fit equally well. Our staging procedure was run using Mathematica (Wolfram Research, Champaign, IL).

2.3.5 Image analysis

Routine analysis, such as tracing the contours for staging, was performed in ImageJ (NIH, Bethesda, MD). More complex image segmentation used either Packing Analyzer [43] or SeedWater Segmenter [44].

2.4 Results and Discussion

2.4.1 External forces on the germband

If the amnioserosa plays an active mechanical role in germband retraction, then the segments of the germband should experience an external force in the direction along which the amnioserosa contracts. The germband reshapes drastically during retraction, so this assessment is best done in a series of local coordinate systems, one for each germband segment, that move with the tissue. In each local coordinate system, the 'y direction' is defined to stretch from the edge of the embryo to the amnioserosa (Figure 2.2*B*, red line), bisecting the angle between the segment's boundaries; the 'x direction' is perpendicular to that (Figure 2.2*B*, blue line). We define the local coordinate systems so that the positive x-direction is the direction of segment motion and the positive y-direction is the direction of the amnioserosa.

To determine if the germband was subject to any external forces, we examined how the tissue reacted to small laser incisions. In each segment of the germband, we made 15-μm line cuts along the x and y direction (Figure 2.2*C*, *D* respectively). In response to each incision, the tissue recoiled from the ablation site, the wound reached a maximum area, and then it began to heal (Figure 2.2*E*). The expansion of these wounds indicates that the segments are under tension; however, it is not enough to tell us if that tension is generated by the amnioserosa.

If the amnioserosa pulls on the germband as previously suggested [13], then the expansion of wounds in the germband segments should be greater in the y-direction than in the x-direction. To emphasize this difference, we compared the maximally expanded

shapes of wounds made in the y-direction to those made in the x-direction. Figure 2.3 shows a simple model of wound expansion for line cuts made in both directions. If cells autonomously expand in the germband, then in each cell there should be a force pushing outward along the direction of elongation (y-direction) and a force pulling in along the x-direction. The result of this set of internal forces would be a wound that expands along the x-direction and collapses along the y-direction. Thus the aspect ratio in this case would be higher for cuts made along the x-direction.

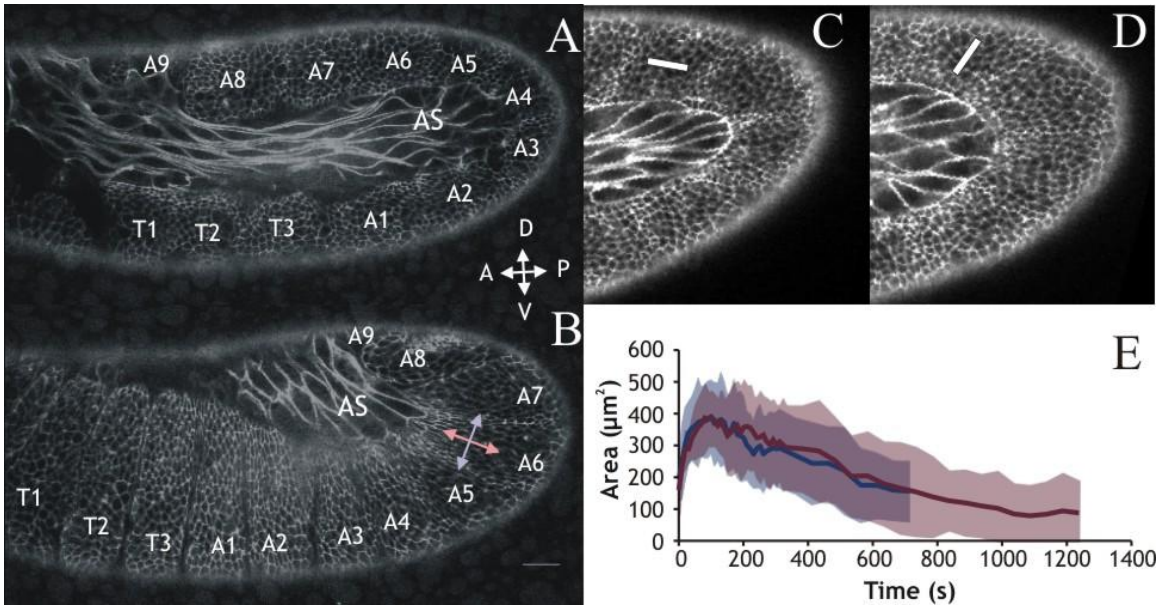

Figure 2.2. (*A*) Lateral view of an embryo in early germband retraction, with the germband segments and the amnioserosa (AS) marked. (*B*) Same embryo late in germband retraction. Anterior is to the left and dorsal is to the top. A local coordinate system is shown for segment A6 where the red axis is in the y-direction and the blue is in the x-direction. (C) 15-µm ablation site along the x-direction in segment A5. (D) Same in the y-direction. (E) Area of the wound versus time for wounds made in the x (blue) and y (red) directions for segment A7. This graph is typical for both directions in all segments. The solid line is the average area and the shaded region denotes one standard deviation (N = 8, 6 for x- and y-aligned wounds respectively).

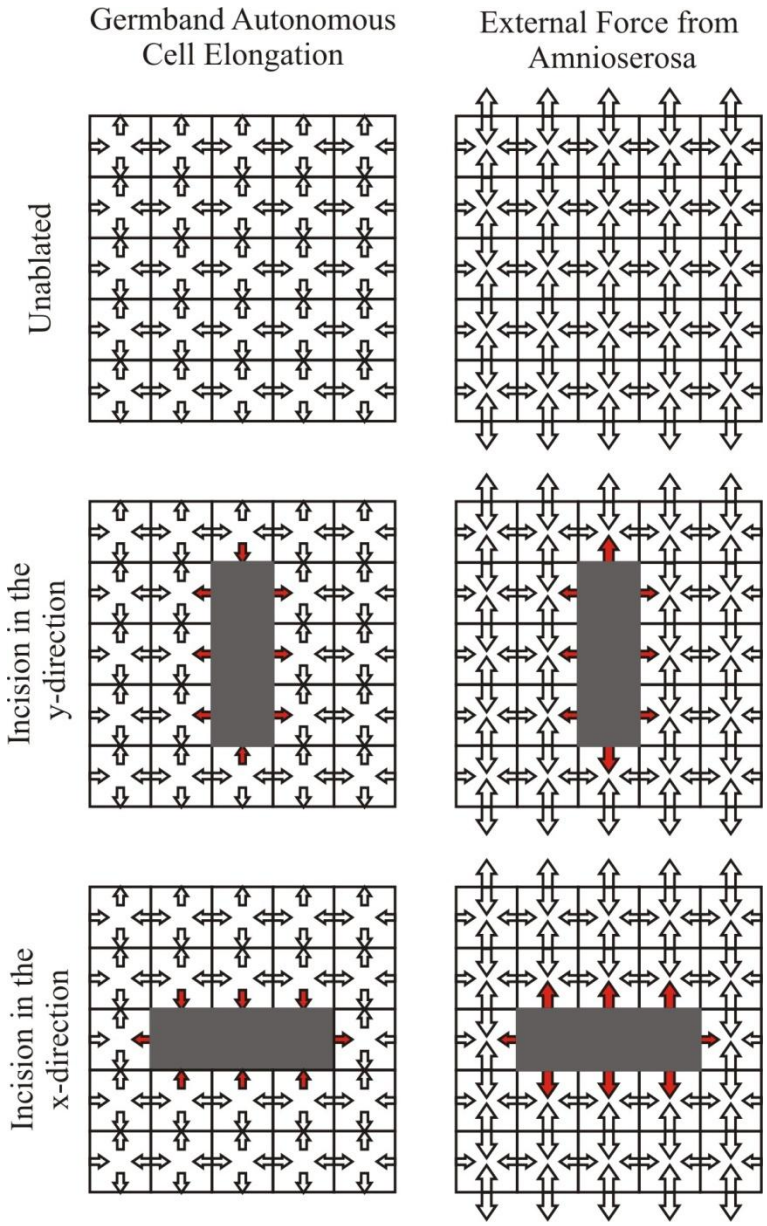

Figure 2.3. Schematic representation of the proposed forces on wound edges in a segment where the cell elongation is either cell autonomous (left) or caused by a pulling force from the amnioserosa (right). In the next chapter a more detailed model of these cuts will be presented.

On the other hand, if the amnioserosa pulls on the cells of the germband to elongate them, each cell will have an internal force in the y-direction that counteracts the force of the amnioserosa to attempt to maintain cell shape. Each cell will also exert a force on the cell below it in the direction of the amnioserosa. Assuming a Poisson ratio between 0 and 0.5, the forces in the x-direction will have the same direction as in the case

of autonomous elongation, but these forces will have a smaller magnitude than the forces along the y-direction. This results in wounds that expand more in the y-direction than in the x-direction. Thus if the amnioserosa pulls on the segment, the wounds' aspect ratios should be higher for those made in the y-direction (Figure 2.3). A more sophisticated model of these incisions will be considered in Chapter 3.

We ablated 15-μm lines in each segment of the germband in both directions Since germband retraction is a dynamic system, forces on the germband may not be constant. We thus selected embryos to wound based on maintaining a uniform average pre-wounding stage (36% retracted) for each segment and direction (see Experimental Methods). Figure 2.4 shows the results of our comparison. The wound sizes at maximum expansion were similar for a given segment between incisions in either direction. In contrast, several segments had significant direction-dependent differences in aspect ratio ($p < 0.05$). These segments (A4, A5, and A7) are in the curve of the germband throughout most of retraction. For each, the largest aspect ratio was for incisions made in the y-direction, consistent with an amnioserosa that pulls on the curve of the germband.

We then performed a similar experiment in the amnioserosa. If the amnioserosa is pulling on segments in the curve of the germband, then cuts made along its long axis should have a higher aspect ratio than cuts made along its short axis. Unfortunately, due to the drastically elongated shape of amnioserosa cells, it is not possible to wound several cells along its long axis with the same cut length used across the short axis. We therefore performed these incisions in sGMCA flies, a strain in which subcellular wounds can be seen in the amnioserosa [1]. As for the germband, the maximally expanded wounds for the two directions were of approximately the same size. Even though the difference

between aspect ratios for the two directions was noticeable, it was not significant ($p = 0.29$), because the long-axis wounds were highly variable.

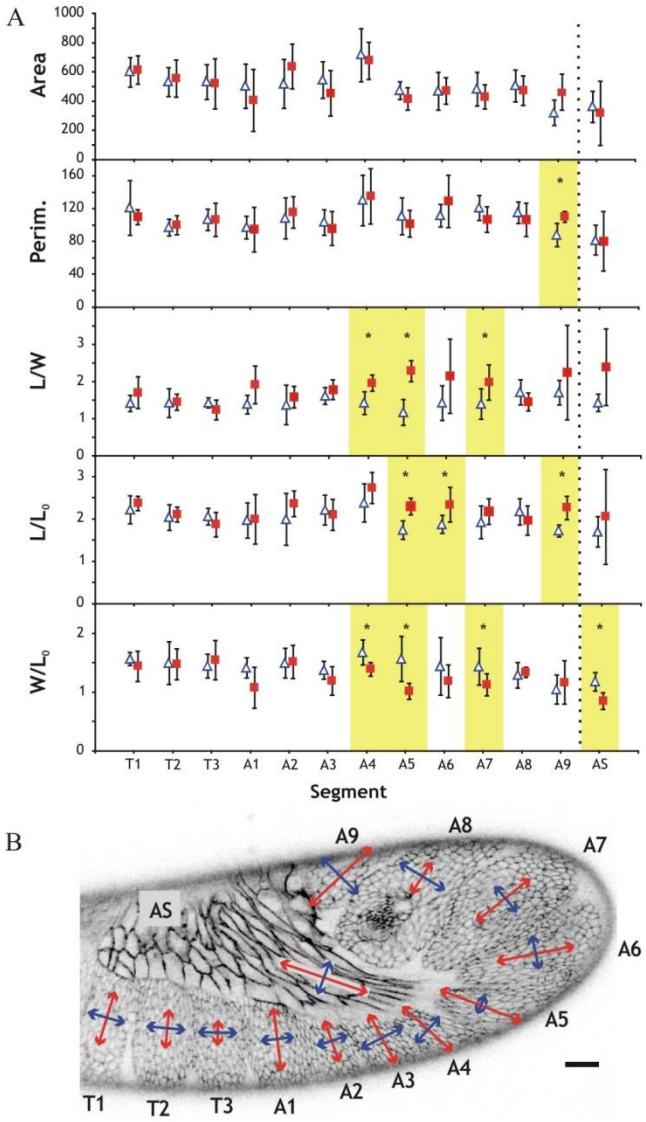

Figure 2.4. Descriptors of maximally expanded wound shapes due to 15-µm line cuts in the germband. Blue denotes incisions made in the x-direction, red in the y-direction. (*A*) Area (µm^2) and perimeter (µm) at maximum wound expansion, followed by graphs of three measures of elongation: aspect ratio, expansion along the cut direction divided by the cut length, and expansion perpendicular to the cut direction divided by the cut length. The shape (triangles, x-direction and squares, y-direction) denotes the average for each ablation set and the bars indicate ± one standard deviation. Where there is a significant difference ($p < 0.05$) between directions in a segment, the data is highlighted and marked with an asterisk. (*B*) Graphical representation of wound aspect ratios overlaid on an embryo at mid-germband retraction. Arrows indicate the aspect ratio of the expanded cut minus 1 (L/W – 1) to emphasize regions with differences in aspect ratio between the two cut directions. Scale bar is 20 µm.

Although the series of 15-µm incisions does not tell us definitively that the amnioserosa pulls on the germband, it does indicate that segments of the germband are not all under the same tensile stress and that the tension observed in segments around the curve of the germband is consistent with a mechanical role for the amnioserosa.

2.4.2 Role of the amnioserosa

To further test the necessity of the amnioserosa for retraction, we conducted another series of ablations in which we destroyed parts of the amnioserosa and noted the effects. Since minor incisions in the amnioserosa can heal, we quantified the progression of retraction using a contour staging method (see Experimental Methods) that is sensitive to even transient disruptions to retraction.

We started with a series of line incisions to destroy the amnioserosa on one lateral side of the embryo (Figure 2.5*A*). Although this leaves the other half of the amnioserosa intact, it was sufficient to halt germband retraction (Figure 2.5*E*, *I*). We conducted additional experiments to visually confirm that the amnioserosa was still intact on the other side. Thus, ablation of half the amnioserosa is sufficient to duplicate the failure of germband retraction observed in *hindsight* mutants in which the entire amnioserosa undergoes premature apoptosis [54].

We then conducted a series of less destructive ablations to determine the relative importance of various sections of amnioserosa – for example, sections close to and far removed from contact with the curve of the germband (Figure 2.5*B*-*C*). Two-line ablations of both regions caused incomplete retraction; however, defects were less severe than the failure caused by destruction of half the amnioserosa (Figure 2.5*J*-*K*).

Interestingly, the largest difference between these two cut designs was the shape of the germband after retraction should have completed. Cuts made in the curve of the germband resulted in a narrower bend than those made closer to the dorsal surface (Figure 2.5*F*-*G*). This is consistent with the hypothesis that the amnioserosa must pull on segments in the curve of the germband for the germband to uncurl.

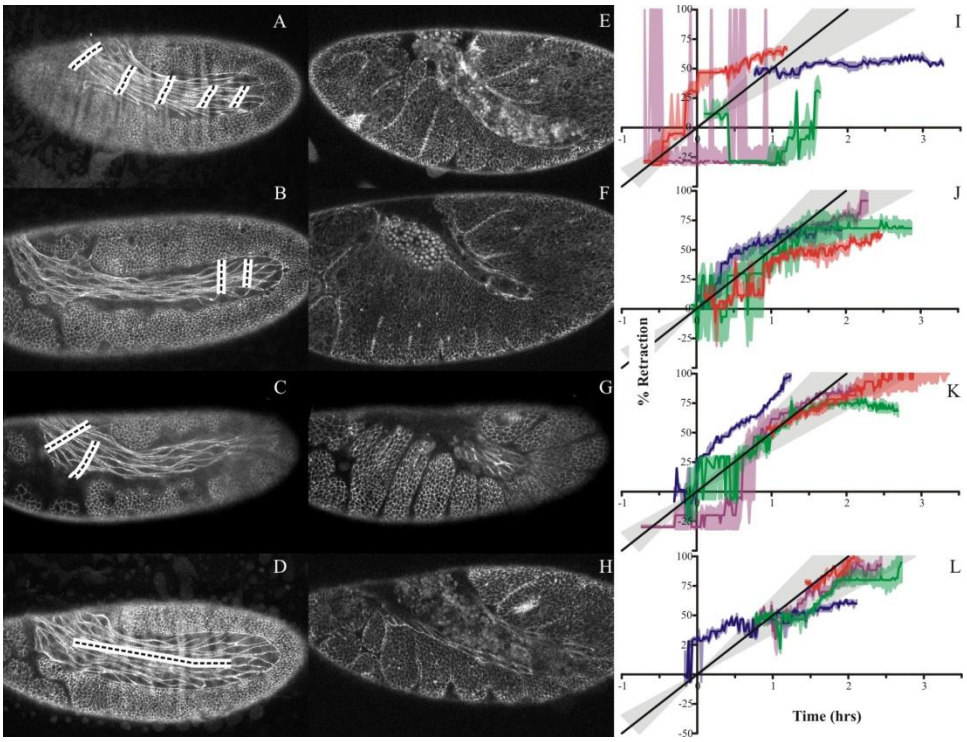

Figure 2.5. (*A*-*D*) Cut designs used to probe the role of the amnioserosa in germband retraction. (*E*-*H*) Same embryos as in *A*-*D*, respectively, but when germband retraction would have completed in an unablated embryo. (*I*-*L*) Staging graphs for each cut design. The black line is the standard retraction curve with the gray region representing ±2σ. Each colored line represents a single experiment and its surrounding colored region represents its staging range. Since the graphs show the percent retraction, lines of about the same slope as the black line are retracting normally. Horizontal lines have stopped retracting.

To test whether this effect is mechanical and not due to an interruption of biochemical signaling between the amnioserosa and germband, we cut along the center of the amnioserosa's long axis, destroying its mechanical integrity, while leaving cells directly adjacent to the germband intact (Figure 2.5*D*). These wounds all caused at least a

transient disruption, typically stalling retraction for about thirty minutes (Figure 2.5*L*). Most of these wounds heal; after wound healing begins, germband retraction tends to resume. The one embryo that did not heal was also the one that never resumed retraction (Figure 2.5*H*, and the blue line in Figure 2.5*L*). These results suggest that the amnioserosa's role is not limited to biochemical signaling from its cells adjacent to the germband; the amnioserosa's mechanical integrity is crucial.

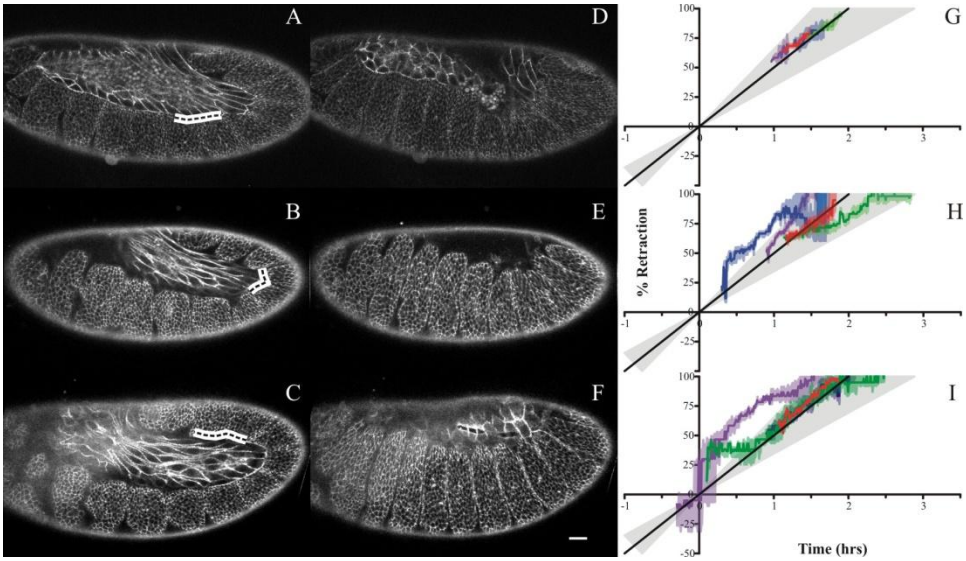

Figure 2.6. Similar to Figure 2.5. (A-C) Cut designs for various small separations between the amnioserosa and the germband. (D-F) Embryos after retraction. (G-H) Staging graphs of each cut design. The black line is the standard retraction curve with the gray region representing ±2σ. Each colored line represents a single experiment and its surrounding colored region represents its staging range. Since the graphs show the percent retraction, lines of about the same slope as the black line are retracting normally.

As a last test to distinguish between a biochemical and mechanical role for the amnioserosa, we considered what happens when signaling is disrupted, but the mechanical integrity of the tissue is left intact. To this end, we ablated along the border between the amnioserosa and the germband (Figure 2.6). These incisions were fairly small and healed quickly. None of these cuts even transiently disrupted retraction.

2.4.3 Germband changes in the absence of retraction

To further decouple the mechanical interactions between the germband and the amnioserosa, we considered what changes occurred in the germband even in the absence of retraction, due to the loss of one lateral side of the amnioserosa (Figure 2.5*A*). Furrow formation occurs normally, despite the lack of retraction (Figure 2.5*A*, *F*). To determine if the germband cells have elongated normally we considered the parameters of a composite cell, with composite area moments

$$J_c = \begin{bmatrix} \frac{1}{n_{cells}}\sum_{cells} J_{xx} & \frac{1}{n_{cells}}\sum_{cells} J_{xy} \\ \frac{1}{n_{cells}}\sum_{cells} J_{yx} & \frac{1}{n_{cells}}\sum_{cells} J_{yy} \end{bmatrix} = \begin{bmatrix} J_{c,xx} & J_{c,xy} \\ J_{c,yx} & J_{c,yy} \end{bmatrix}. \quad (2.1)$$

This then allows us to define a composite aspect ratio κ for the collection of cells, where

$$\kappa = \sqrt{\frac{J_{c,max}}{J_{c,min}}}, \quad (2.2)$$

and a composite elongation direction,

$$\alpha = 90° \left(1 - \tfrac{1}{\pi}\tan^{-1}\left(\frac{2J_{c,xy}}{J_{c,yy} - J_{c,xx}}\right)\right). \quad (2.3)$$

These were calculated per segment based on the segment axes defined above, so the angle has the same meaning within the segment regardless of the segment's position in the embryo.

At the start of retraction, the composite κ for segments along the curve and ventral side of the embryo is very close to 1.2 (1.18 for four control embryos (c), 1.23 for four embryos in which the amnioserosa will be ablated (a)). The composite κ is lower than the aspect ratio for the individual cells (~1.5) because it takes into account both the elongation of the cells and their alignment, which is weak early in retraction (Figure 2.7). By late germband retraction in the control embryos, κ increases to 1.48 in control

embryos, but remains at 1.23 when the amnioserosa has been ablated. To investigate this further, we looked separately at segments in the curve (A5, *N*=2) and those on the ventral side (A2, *N*=2). The segment in the curve has a late retraction κ close to 1.4 for both ablated and unablated embryos (a: 1.38 for both and c: 1.44 and 1.50). This indicates that cell elongation occurs normally in the segment along the curve of the germband without a complete amnioserosa, and in the absence of retraction. The orientation may be affected by removing half of the amnioserosa; in one of the two experiments, elongation is not oriented towards the amnioserosa as it is in unablated embryos (Figure 2.7*A*). These results suggest that cell elongation in this segment is germband autonomous, and verifies that it is insufficient for retraction.

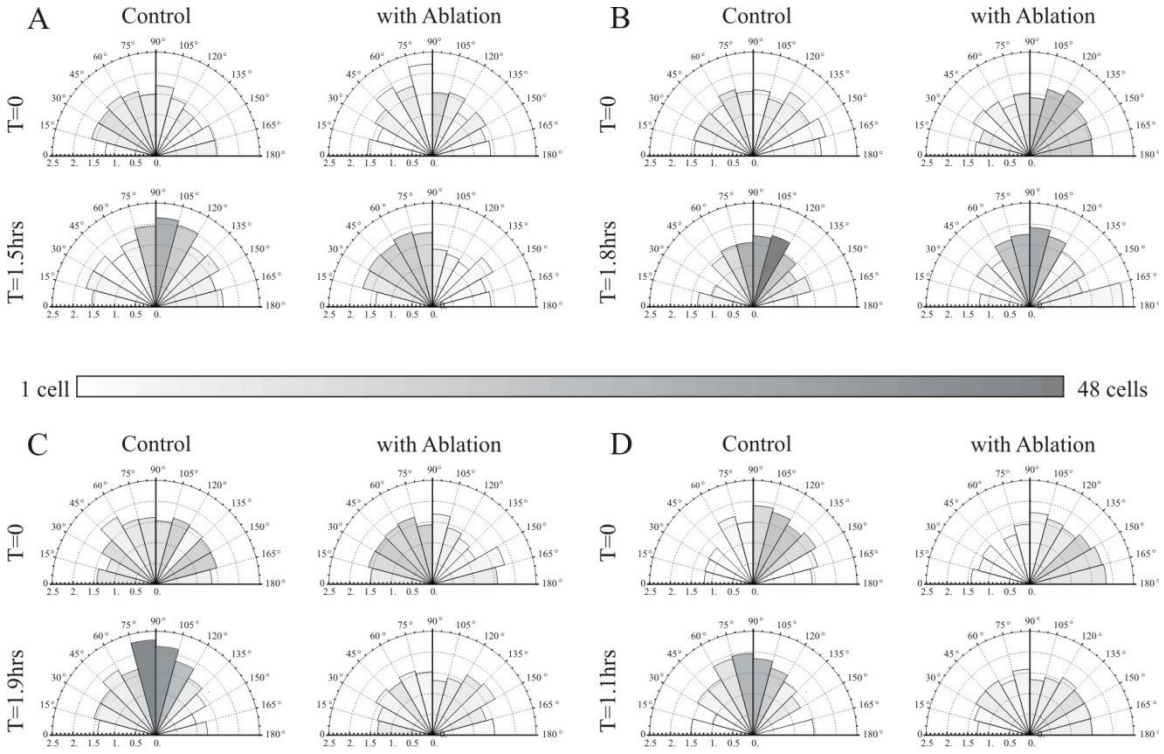

Figure 2.7. Each wedge represents the average aspect ratio for all cells that fall within that angle range. The color of the wedge indicates the number of cells within its angle range as specified by the scale bar. Each set of 4 are two time matched experiments, one without ablation and one where half of the amnioserosa is ablated. (*A*, *B*) from segment A5 and (*C*, *D*) from segment A2.

For the segment on the ventral side, the late retraction κ (a: 1.04 and 1.10 and c: 1.52 and 1.47) is smaller than the value early in retraction in the ablated embryos (a: 1.22 and 1.33 and c: 1.08 and 1.22). Since κ is a measure of both elongation and alignment, we looked at the average aspect ratio of cells on the ventral side, to see if elongation changes or just the alignment. The aspect ratio also decreases, so it is cell elongation that has changed (Figure 2.7*C, D*). Thus, the same changes that were cell autonomous in the curve of the germband may be dependent on the presence of the amnioserosa in segments on the ventral side of the embryo. It is also possible that the changes in the cell shape on the ventral side are due to additional forces caused by the lack of retraction, *e.g*. increased tension in the x-direction due to a lack of motion in more posterior segments.

2.4.4 Behavior of isolated germband cell patches

To further investigate the cell autonomous changes in the germband, we looked at a patch of germband cells separated from their neighbors using laser microsurgery (Figure 2.8*A, B*). Initially many of the isolated cells will fade away in the first several minutes, accounting for much of the observed loss in patch area and change in shape (Figure 2.8*C*). Within 20 minutes after this sort of incision, isolated cell patches will either fade away completely (*N*=9 of 21) or reattach (*N*=12 of 21). In general, those that faded away had fewer cells than those that reattached; however, even large patches completely faded when those patches were isolated from the curve of the germband. Of the patches imaged along their depth, reattachment typically occurred basally first. These patches travel at about the same rate as the rest of the tissue, reattaching to the wound edge in the positive x-direction as often as to the one in the negative x-direction (*N*=5 of

10 for each). Of these, most attach to the center of the wound edge (*N*=4 of 10), while the rest reattach with the same frequency to the wound corner in the positive y-direction as to the one in the negative y-direction (*N*=3 of 10 for each).

Before considering the cell shape changes observed in isolated patches, we need to consider the cell shape changes that normally occur in the same tissue over similar time scales. Germband cells elongate from aspect ratios of ~1.5 to ~1.8 over the two hours of retraction. Such slow changes would not be detectable over the 20 minutes that patches remain isolated from the rest of the tissue. On the other hand, this time should be sufficient to see shape relaxation if germband cells have been elastically stretched by external forces. We detected no changes in cell area, volume, and aspect ratio in the isolated patches, even in patches of previously elongated cells. This suggests that the germband cells at least have a mechanism for holding their elongated shape.

The only difference we found in the separated patches was a change in the cells' apicobasal wedging. We measured this wedging from time-resolved images at different focal planes based on the slope of cross-sectional area versus depth (Figure 2.8*D-G*). Using this measure, we find a wide range of positive and negative wedging in segment T2 prior to germband retraction. The cells collimate as germband retraction begins and remain that way in unablated embryos for the first 15 minutes of retraction (Figure 2.8*D, E*). In separated patches, by the time the cells reattach, they are wedged, such that they are predominately smaller on the apical surface (Figure 2.8*G*), consistent with the patches reattaching basally first. Taken all together, the patch cuts are highly suggestive that some of the changes in the germband (cell shape, segment motion) are autonomous, but remain inconclusive.

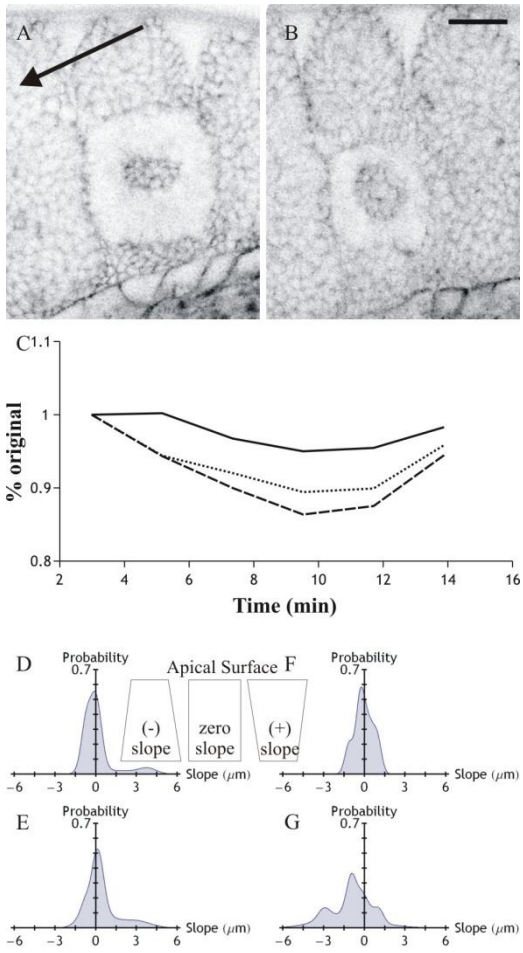

Figure 2.8. (*A*) A separated patch 5 min after ablation. Arrow indicates the direction of tissue travel. (*B*) The same patch 16 min later. The scale bar in *B* applies to both images and represents 20 µm. (*C*) Changes in the average planar cell area in isolated patches (solid line), the average cell number (dotted line), and average patch size (dashed line) normalized by the first frame post-wounding. *D-G* show the probability density for cells' apicobasal wedging based on the slopes of area vs. depth. Inset: a cartoon of a cell's lateral cross section, illustrating the wedging represented by different slope values in *D-G*. (*D*, *E*) Control data from segment T2. (*F*, *G*) compiled from 3 patch cuts made in segment T2 early in retraction. (*C*) As retraction begins, and (*D*) approximately 15 minutes into germband retraction. (*F*) Cells just prior to wounding at the beginning of retraction and (*G*) as they first reattach approximately 15 minutes later.

2.5 Conclusions

Our observations suggest an interesting model for germband retraction, one in which both tissues play a role. The mechanical integrity of the amnioserosa is necessary

for successful germband retraction, but is not responsible for furrow formation between germband segments or all of the germband cell shape changes. Only segments in the curve of the germband show evidence of an external force in the direction along which the amnioserosa cells contract, and yet in these segments cell elongation occurs normally in the absence of half of the amnioserosa. Our isolated patch experiments indicate that germband cells maintain their shape in the absence of external forces, but cells on the ventral side lose their elongation in the absence of an amnioserosa flank. This suggests that their loss of elongation is not due to a loss of external stress. Together these lend credence to a model where much of the germband changes are autonomous, but where the amnioserosa assists uncurling of the germband by pulling on segments in the germband's curve.

Interestingly the segments of the germband cannot be considered to behave as a single entity. The segments around the curve of the germband behave quite distinctly from the rest of the tissue. More work is needed to explore the differences between segments, and will be undertaken in the next chapter via a finite-element model.

CHAPTER 3

GERMBAND RETRACTION: USING MODELING TO UNDERSTAND MORPHOGENESIS

3.1 Abstract

Our previous experiments in germband retraction (Chapter 2) demonstrate that the mechanics of the germband vary from segment to segment. Although most of this tissue responds isotropically to laser-induced wounds, segments in the curve of the germband demonstrate a pronounced anisotropy. To understand the physical causes of this distinct behavior, we use a finite-element model to investigate how a tissue's wound response varies with its mechanical environment. We explore cell sheet behavior under a range of anisotropic external stresses and polarizations of cell edge tension, where the cell polarization axis is either parallel or perpendicular to the principle stress direction. Within this parameter space, we identify the regions that best match the cellular and wound anisotropy for each segment. All but three germband segments are fit best when the principle external stress direction is perpendicular to the axis of cell polarization. The exceptional segments are best fit by either isotropic external stress or unpolarized cells. Around the curve of the germband, external stress is dominant, *i.e.*, it determines the direction of cell elongation. In most other segments, cell polarization dominates. These results confirm that the amnioserosa pulls on segments around the curve of the germband; however, they also suggest that cell polarization is not simply directed towards the amnioserosa. Instead, our results are consistent with a mechanical cue for cell

polarization, one where the polarization aligns perpendicular rather than parallel to the direction of greatest stress.

3.2 Introduction

During germband retraction, many changes occur in segments of the germband. The cells elongate, and many segments move dramatically across and around the posterior end of the embryo. Through previous experiments, we found key roles in germband retraction for both anisotropic stress and cell autonomous elongation (discussed in detail in Chapter 2). The amnioserosa physically pulls on at least some germband segments – likely generating greater tension in the direction of the amnioserosa. Nonetheless, isolated patches of germband cells maintain their slightly elongated shape, indicating at least autonomous shape maintenance. Furthermore, in some of the segments, cells still undergo their normal elongation even after ablation of one entire flank of the amnioserosa. Here, we use computational modeling to determine exactly how anisotropic stress and autonomous cell elongation contribute to the mechanical environment of each germband segment.

We do so by modeling the series of 15-μm line incisions discussed in Chapter 2 using a well established technique that has successfully modeled cells and tissues – the cell-level finite-element method [6,45-51,58]. We model cells as two-dimensional polygons with a viscous and incompressible cytoplasm and edge tensions that can vary with edge orientation. With this orientation dependence, we can polarize the edge tensions to drive autonomous cell elongation. Non-autonomous elongation can be

modeled by applying anisotropic external stress to the edges of a simulated cell sheet. With this model, we can thus explore the varying contributions of cell polarization and anisotropic external stress to the expansion of linear incisions.

We find that the finite-element model reasonably reproduces both cell elongation and wound expansion, but, for most segments, only when the external anisotropic stress works against cell autonomous elongation. For segments in the curve of the germband, cells elongate in the direction of greatest external force – consistent with the amnioserosa pulling on these segments – but are polarized in a perpendicular direction. For most other segments, cells elongate in the direction dictated by their edge-tension polarization. Interestingly, these polarizations are not aligned in a common direction for all segments, neither towards the amnioserosa nor dorsoventrally.

3.3 Model Details

3.3.1 Length and time scaling

To facilitate comparison of simulations and experiments, we simulate cell sheets with the same cell size and density as found experimentally. Specifically, we match the spatial scale factor ρ = (total edge length)/(total sheet area) [47], which allows direct comparison of distances and areas between experiments and simulations. To do so, we simulate 45x100-μm sheets with 300 cells. These sheets are purposely wider than actual germband segments to reduce boundary effects, especially under conditions with highly elongated cells. They are rectangular to conserve computational resources. We run

simulations on seven cell sheets with the above characteristics, but different cell geometries (based on Voronoi tessellation of randomly chosen seed points).

We cannot as readily equate experimental and simulated time scales. Instead, we run simulations at a given viscosity and later match the simulations' time scales to experiments using two identifiable events: the time of ablation and the time at which an expanding wound reached 90% of its maximum size. The time of ablation is easily identified in simulations and to a lesser extent in experiments. In the simulations, $T = 0$ steps occurs immediately after the wound is made, but before it starts to expand. In experiments, ablation of a 15-μm line is not instantaneous, but takes ~ 2 s. Since tissue starts to move right after the first ablation pulse, we assign $t = 0$ s to the image frame prior to ablation, even though this is not precisely when wounding occurs. The point at which a wound reaches 90% of its maximum expansion (t_{90}) is a straightforward calculation for experiments in which wounds reach a maximum area and then shrink as they begin to heal (Figure 2.2*E*). Our simulations do not include a wound healing response, so each wound expands asymptotically towards its true maximum. We therefore calculate an effective maximum area based on the time at which the relative change in area between successive unit time steps ($\Delta A/A$) is first less than 1×10^{-4}. The corresponding area is taken as an effective maximum area and used to find the simulation's T_{90}. We then scale the simulated times to match the experiments using the factor t_{90}/T_{90}.

3.3.2 Model elements

Previous work has demonstrated that tissues in *Drosophila* embryos act largely as continuous sheets [1], *i.e.*, tensions along cell-cell interfaces bear less than ~30% of the tissue-level stress. We thus fix the average external stress $\bar{\sigma}$ to 3× the amount carried by cell edge tensions. Anisotropic external stress is applied by setting $\sigma_1 = \bar{\sigma} + \Delta$ and $\sigma_2 = \bar{\sigma} - \Delta$, with the degree of anisotropy given by

$$\frac{\Delta}{\bar{\sigma}} = \frac{\sigma_1 - \sigma_2}{\sigma_1 + \sigma_2}. \tag{3.1}$$

To promote autonomous cell elongation, we allow the cell edge tensions, γ, to vary with edge orientation according to

$$\gamma(\theta) = \gamma\left(1 + \frac{f}{2} - f\cos^2\theta\right), \tag{3.6}$$

where f is the polarization factor (0 to 2) and θ is the angle of each cell edge relative to a global polarization axis. With this, cells tend to elongate along the global polarization axis (Figure 3.2).

In addition to the line tension γ, each cell edge also carries a viscoelastic truss element. These elements prevent wounds from expanding indefinitely. We use the simplest element that yields wound behavior similar to experiments, a Kelvin-Voigt model (spring and dashpot in parallel). To determine appropriate parameters for the spring and dashpot, we matched simulations of wound expansion under isotropic external stress to experiments in which wound expansion did not depend on the incision's orientation. These parameters are used for all truss elements in all subsequent simulations.

At each step in the simulation, there may be small changes in area for individual cells due to approximations in the numerical solutions. Since cells in the germband do not

undergo large changes in size during retraction, the model includes an area constraint for each cell, attempting to reverse any changes in cell area over five time steps. This constraint is implemented as a Lagrange multipier and physically represents an isotropic cell-internal stress or pressure. In addition, since neighbor exchanges are uncommon during germband retraction [13], such rearrangements are not allowed in the model.

With the above elements, we simulate a wound by releasing the area constraint on any wounded cells (equivalent to setting cell-internal pressure/stress to zero), setting the cell edge tensions between wounded cells to zero, and removing the viscoelastic truss elements from any wounded edges. To mitigate boundary effects, we did not wound cells within three cells of a boundary.

To make consistent line cuts, even in cell sheets with highly elongated cells, we calculated the number of cells along a 15-μm line in each direction for each cell sheet, using the average number of cells in each direction, as well as the sheet's dimensions after being annealed with its polarization and external stress. We then wounded a straight line with a length determined by the calculated number of cells. Since cells are not always packed end to end, most simulated wounds, as in the experiments, are more than one cell wide at some point along the 15-μm line.

3.3.3 Software

Finite-element models were run on custom software developed by G.W. Brodland's group at University of Waterloo [45,46,48,51]. Statistical analysis and plotting were done in Mathematica (Wolfram Research, Champaign, IL).

3.4 Results and Discussion

3.4.1 Parameter space

In our simulations, we explore a four quadrant parameter space of cell polarization and external stress anisotropy, replicating the experimental per-segment axes by defining a parameter as positive if it acts vertically. Figure 3.1 illustrates the relationship between polarization and anisotropy in each segment. In the first and third quadrants, the global polarization axis aligns with the principle stress direction; in the second and fourth, they are perpendicular. An experimentally relevant patch from the second and fourth quadrants is shown in Figure 3.2, illustrating the directional differences in external stress and edge tension.

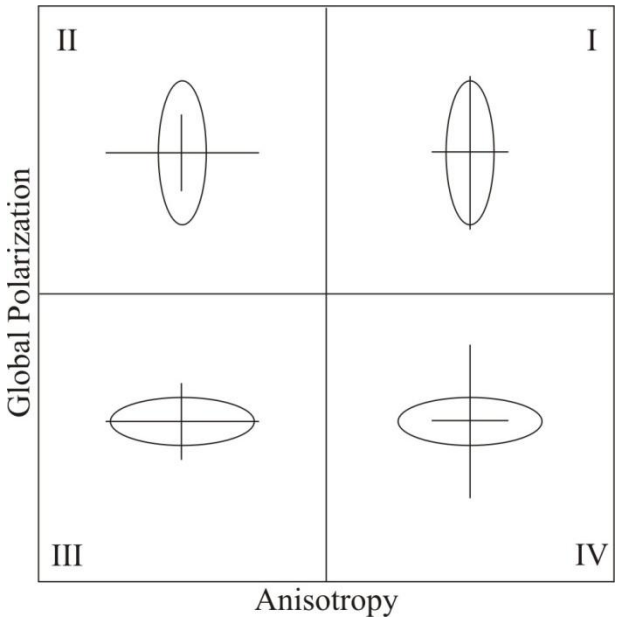

Figure 3.1. Explored parameter space divided into quadrants. Long direction of the ellipses represents the direction that cells would elongate due only to their applied global polarization, while longest direction in the cross hairs indicate the direction that external anisotropic stress would elongate the cells if acting on its own.

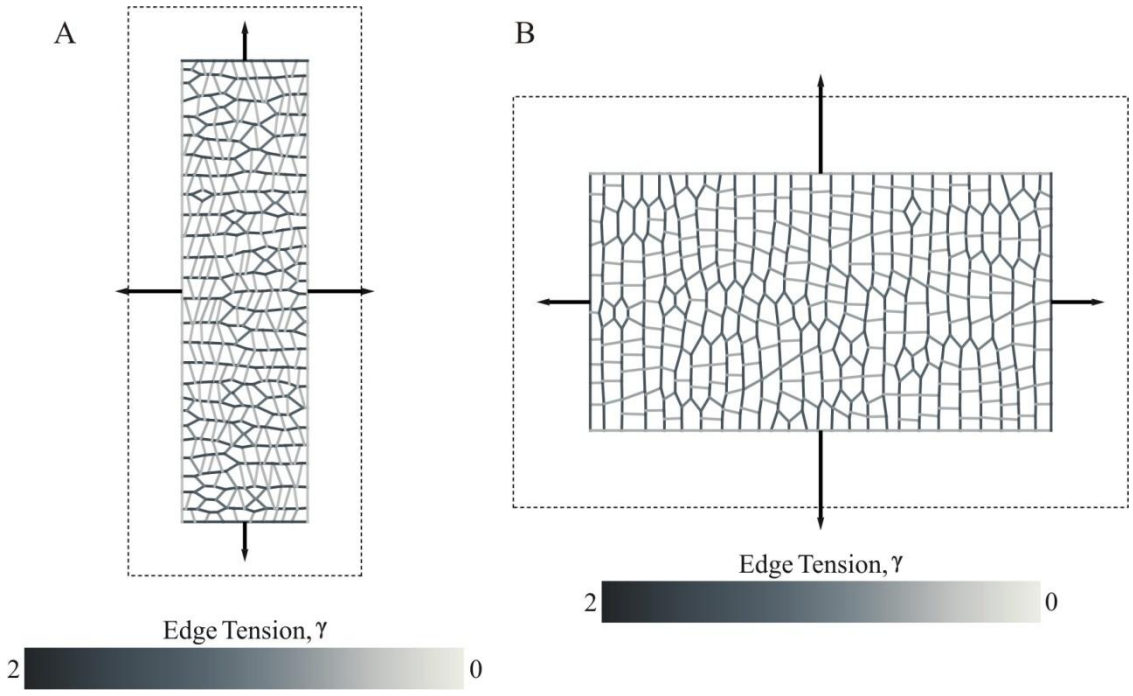

Figure 3.2. A simulated cell sheet with κ_{cells} = 1.31, close to the experimental value 1.33, in (*A*) a polarization dominated patch (quadrant II) and (*B*) an anisotropy dominated patch (quadrant IV). Grayscale denotes edge tension and arrows indicate the relative external stress applied to each edge. Cells elongate in either the direction of greatest stress or least edge tension, depending on the dominant parameter.

Throughout explored parameter space, we wound cells along a 15-μm line in both the x and y directions in each of seven simulated patches. Figure 3.3 shows the expansion of these wounds under four conditions: anisotropic external stress, global polarization, both anisotropic stress and global polarization when anisotropic stress dominates, and both when polarization dominates. The differences in wound are less severe using this model than for those predicted earlier in Figure 2.3 for anisotropic stress versus global polarization. The earlier, simpler model did not place all of the cells under tension and thus had a more severe difference in force distribution along the wound edges.

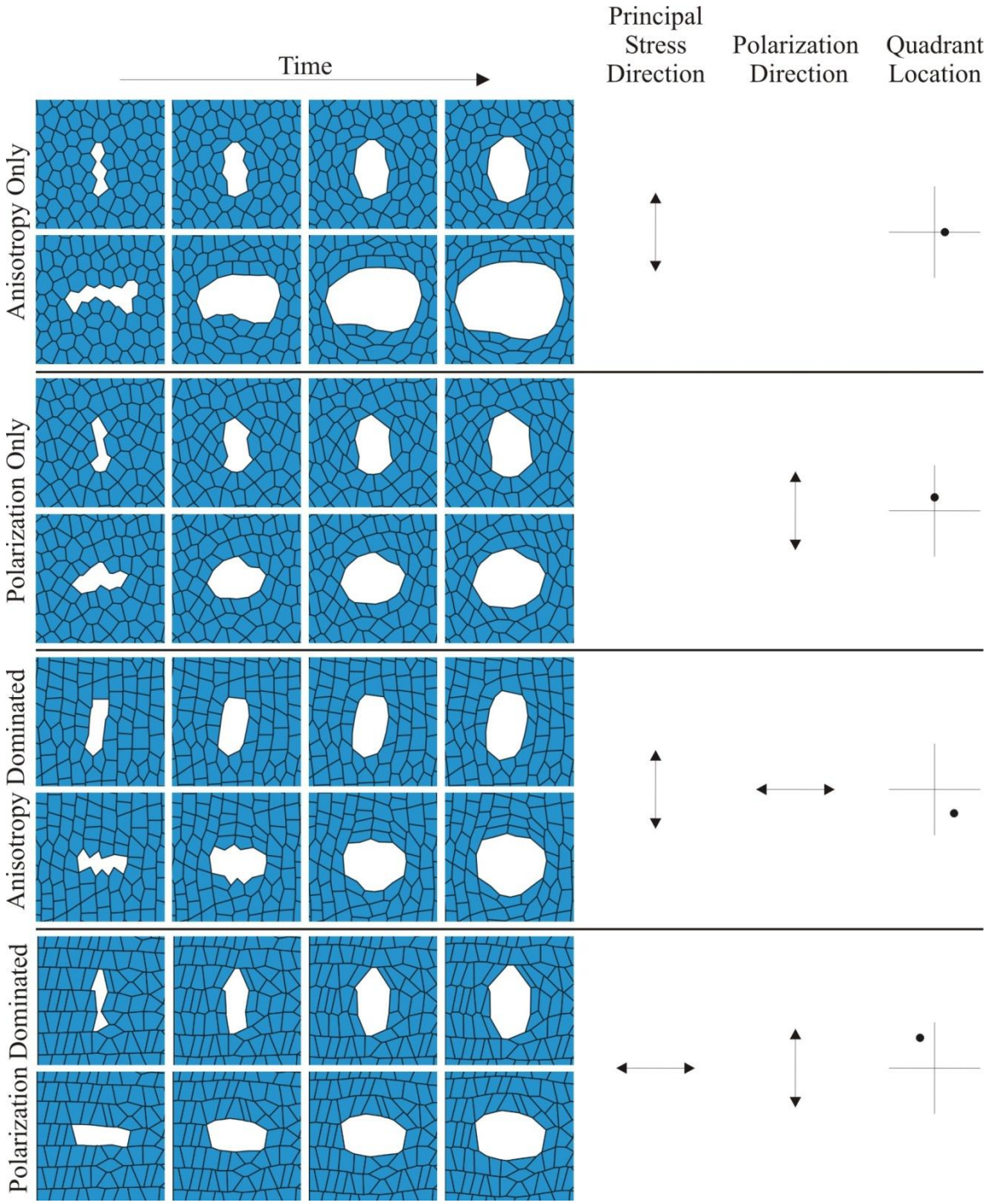

Figure 3.3. Time series of simulated wounds under four patch conditions as marked. κ_{cells} for all patches is close to the experimental value of 1.33. First four columns are times when the wound reaches certain changes in area (ΔA): 0, 1/3 ΔA_{max}, 2/3 ΔA_{max}, and ΔA_{max}. For all wounds the 'amnioserosa' is located along the top edge. To the right of each set of images is an indication of the principal stress direction, cell polarization direction, and where each patch falls in parameter space

Even though each patch has a similar composite κ_{cells} (equation 2.2), the wounds vary in smoothness and anisotropy depending on the applied conditions (Figure 3.3). Therefore we compare the simulations to germband segments via three measurements: κ_{cells} and κ for the maximum expansion of line incisions in both x and y directions, $\kappa_{w,x}$ and $\kappa_{w,y}$. In every germband segment, $\kappa_{cells} \approx 1.33$, while $\kappa_{w,x}$ and $\kappa_{w,y}$ vary by segment, ranging between 1.18 and 1.72 for $\kappa_{w,x}$ and 1.24 and 2.29 for $\kappa_{w,y}$. The simulation values for κ_{cells} , $\kappa_{w,y}$, and $\kappa_{w,x}$ vary through parameter space as illustrated in Figure 3.4.The regime that matches experiments for κ_{cells} extends along a narrow region from quadrant II to quadrant IV with only a small portion crossing quadrant I. For $\kappa_{w,y}$, the experimental values also fall along a line from quadrant II to quadrant IV, but with a larger region crossing quadrant I and a small amount touching quadrant III. The regime that matches experiments for $\kappa_{w,x}$ is distinct from the other two. Although it falls along a similar line between quadrants II and IV, it also has another distinct fit regime in quadrant III.

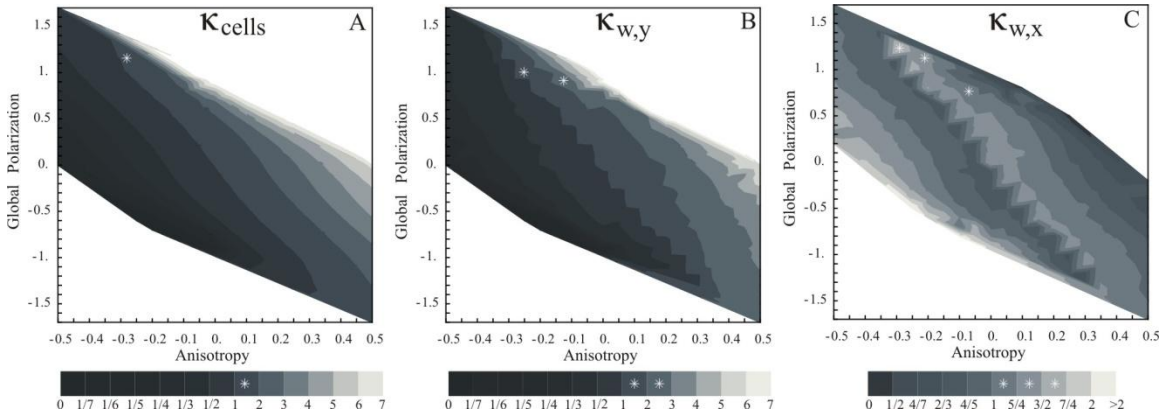

Figure 3.4. Plots of the values of (*A*) cells' composite κ and maximum wound κ for line incisions made (*B*) along the y-direction and (*C*) along the x-direction throughout explored parameter space. Only points where at least five patches annealed are used. Bars below indicate the variable range per color. White stars mark the shaded contours within which experimental values fall.

3.4.2 Germband segment fits

To determine each germband segment's fit region and best fit point, we used a χ^2 test that considered the fit of all three κ's at each point in parameter space (Figure 3.5). Using this test, only segment T3 is best fit by unpolarized cells. Two other segments have their best fit under isotropic external stress (T2 and A8). The fit region for only three segments (T2, A2, and A8) includes quadrant I, where global polarization acts along the principle stress direction, and these do not have their best fit in this region. Thus in most germband segments, cell polarization works against the principle stress direction. The best fit point for most segments (T1, A1, A2, A3, A4, and A7) falls in quadrant II, where cells elongate along the global polarization axis and perpendicular to the principle stress direction. This is consistent with autonomous cell elongation towards the amnioserosa, while the whole segment experiences stress from its connections to neighboring segments as it moves and narrows.

In a few of these segments (A1, A4, and A7), the majority of the fit region actually falls in quadrant IV, where cells elongate along the principle stress direction. Three more segments (A5, A6, and A9) have their best fit, as well as the majority of their fit region, in this quadrant. These six segments all have a noticeably higher aspect ratio for cuts made in the y-direction (Figure 2.4), though the difference is only significant in three of them (A4, A5, and A7). Fits in quadrant IV are consistent with the amnioserosa pulling on the segment, but interestingly cell polarization must act against this force.

To elucidate what these fit regions suggest about germband retraction, we consider their spatial distribution by dividing them into three categories (Figure 3.6): large fit regions in quadrant II and IV (blue); large fit region in quadrant IV, but best fit

in quadrant II (magenta); and best fit in quadrant IV (red). The segments around the curve of the germband fall in the red and magenta categories.

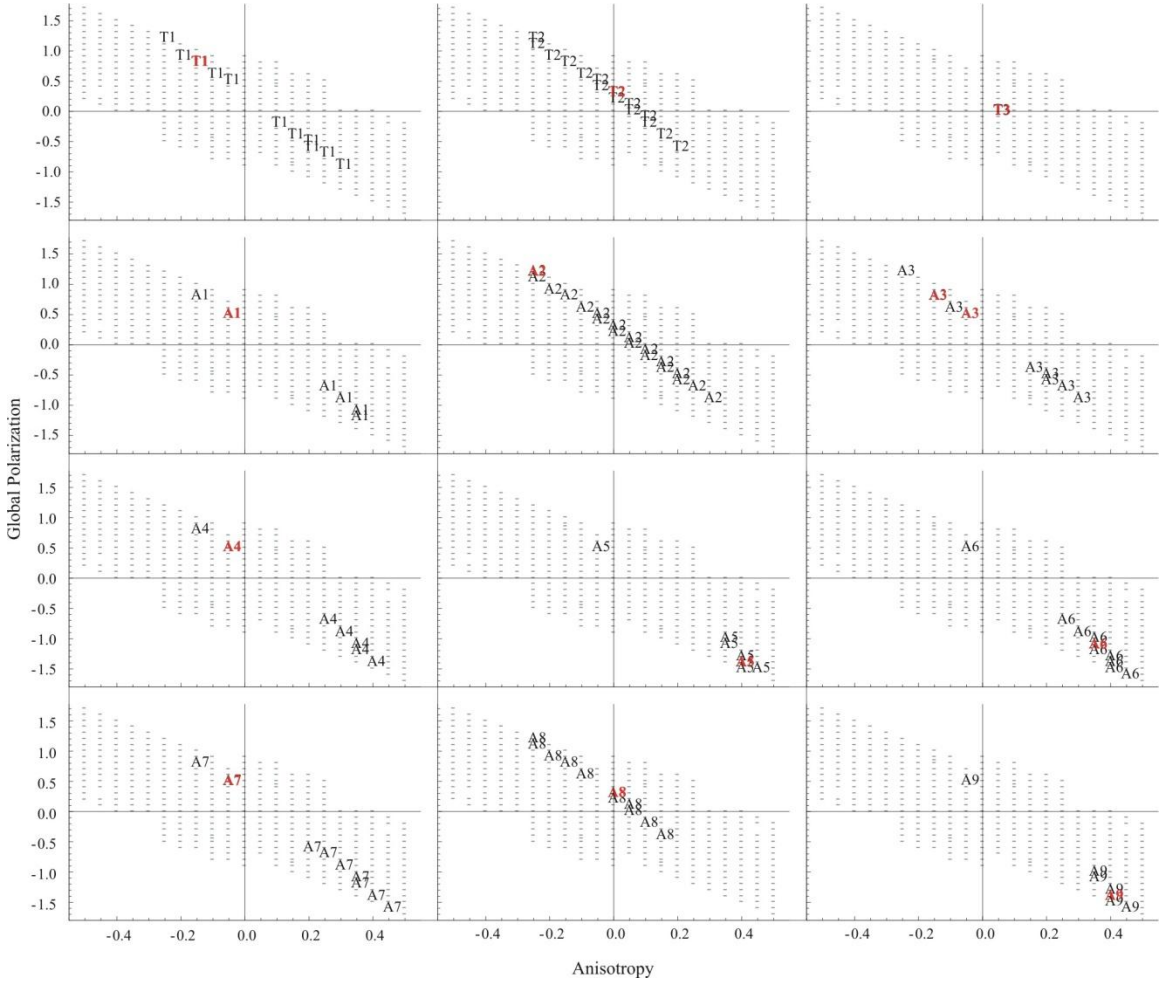

Figure 3.5. Plots of each germband segment's fit region, based on κ_{cells}, $\kappa_{w.x}$, and $\kappa_{w,y}$. Points where the χ^2 value indicates a good fit ($p \geq 0.05$) are marked with a segment label, red for the best fit. Dashes indicate the rest of the explored points.

The external stress distribution is unsurprising, since it aligns well with the results from our previous experiments (Chapter 2); however cell polarization does not always align along the y-direction and thus is not simply directed towards the amnioserosa, as previously expected. It also does not align along a global axis, since cells in segment A9

likely polarize in the anterior-posterior direction instead of dorsoventrally as is probable in most other segments, though most segments are not highly constrained to one polarization direction. Thus we consider two additional models for cell polarization: genetic pre-programming and a mechanical cue.

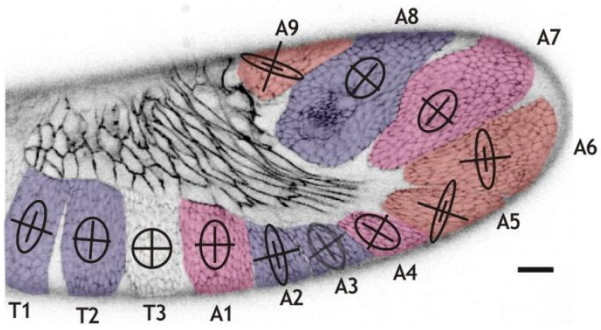

Figure 3.6. An image of an embryo, mid-germband retraction. Ellipses and cross hairs denote each segment's best fit, where the ellipses' major and minor axes are proportional to 1+f/2 and 1-f/2, respectively and cross hairs are proportional to the applied stress in each direction. Colors denote the fit type. Segments with large fit regions in both quadrant II and IV are blue. Segments with their best fit in quadrant II, but with their largest fit region in quadrant IV are magenta. Segments with their best fit in quadrant IV are red. T3 has a unique fit region, so remains uncolored (Figure 3.5). Scale bar indicates 20 μm.

If differences in polarization direction are due to a genetic pre-programming, segment A5 would not have almost normal cell elongation in the absence of an entire amnioserosa flank (Figure 2.7). Under reduced anisotropic stress in the y-direction, cells responding to a pre-programmed polarization axis should either have significantly reduced elongation or elongate along their polarization axis (x-direction). On the other hand, if the polarization axis aligns perpendicular to the principle stress direction, almost normal cell elongation in segment A5 in the absences of an amnioserosa flank is possible. Under the amnioserosa's reduced pulling force, the principle stress direction would switch as the segments anterior to A5 attempt to continue retracting. Thus cell

polarization would switch direction in these embryos based on the angle segment A5 makes with its neighbors, explaining why these cuts sometimes lead to different cell elongation orientations. If polarization aligns perpendicular to the principle stress direction, cell elongation in segment A2 should occur normally after ablation, since its principle stress direction remains unchanged; however its cells actually lose their elongation. If the stress increases along its principle direction due to increased resistance from segments no longer able to retract, this increased stress could pull against the cell polarization enough to create a κ_{cells} close to 1.

3.5 Conclusions

The finite-element method reasonably reproduces germband segments' responses to line incisions; however, for most segments, only when the global polarization axis is perpendicular to the principle stress direction. Consistent with the experiments in Chapter 2, anisotropic stress is dominant only in a handful of segments, most along the curve of the germband. In the rest, cell polarization dominates. Interestingly, our results are consistent with a mechanical cue for cell polarization, one where polarization aligns perpendicular to greatest stress. Fitting line-cut expansions in *hindsight* mutants, where the amnioserosa cells apoptose as germband retraction begins, could verify this model and lead to new insights.

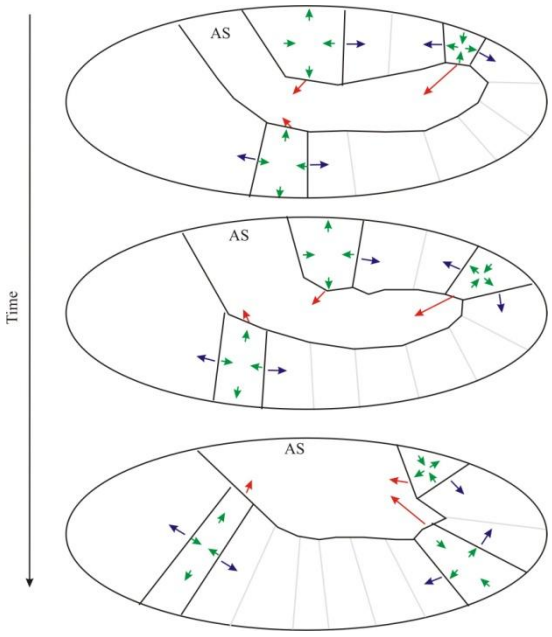

Figure 3.7. Model of germband retraction. Forces on segments T1, A5, and A8 are illustrated. The green arrows indicate forces internal to the segment, blue arrows represent forces from neighboring segments, and red arrows indicate forces on the segments from the amnioserosa. Many of the changes in the germband can occur autonomously, but a pulling force from the amnioserosa helps segments successfully travel around the bend in the tissue.

Figure 3.7 presents our current model of germband retraction, combining the insights from Chapters 2 and 3. In all segments except those around the curve, the movement of segments and their elongation are independent of the amnioserosa. For segments along the germband's curve, the amnioserosa provides a tensile force, which changes direction through time, to assist moving those segments around the posterior bend. Through this mechanism, the amnioserosa assists in uncurling the germband.

CHAPTER 4

DORSAL CLOSURE: THE MECHANICS OF THE AMNIOSEROSA

The work in this chapter is the compilation of two of my publications [1,6] with an emphasis on my contributions – primarily characterizations of the apical actomyosin mesh and investigation into its possible role as a carrier of tension during apical constriction.

4.1 Abstract

Laser hole-drilling is used to investigate the cell-level mechanics of the amnioserosa – a morphogenetically crucial epithelium on the dorsal surface of fruit fly embryos (*Drosophila melanogaster*) – with emphasis on the apical constriction of its cells. We ablate a subcellular cylindrical hole (1 μm in diameter) that passes clean through the one cell layer thick epithelium to assess the mechanics during development – *in vivo* and with subcellular resolution. The mechanical behavior of this epithelium falls between that of a continuous sheet and a 2D cellular foam (a network of cell interfaces), where tensile stress is carried both by cell-cell interfaces and by the cells' apical actin networks. The recoils from single and double wounds are well reproduced when a fine pre-stressed mesh of viscoelastic rods parallel to the apical and basal membranes of the cell are added to a base finite-element model.

4.2 Introduction

The ultimate causative factor in biological development is genetics, but the proximate cause of morphogenetic movements is physical – namely, coordinated changes in the mechanical state of individual cells. When developmental mechanics are considered, the normal course is for physical scientists to develop computational models [45,46,58-64]. These models certainly reproduce the shapes and forms of morphogenetic episodes, but the solutions are generally non-unique [58]. Such models are to be challenged and refined with complementary experiments [65]. In the past decade, laser microsurgery has emerged as a primary means of model validation [4,5,24,55,56,66-69]. Here, we show that a variant of microsurgery, referred to as laser hole-drilling, can elucidate the subcellular stress distribution during a specific episode of morphogenesis – the apical constriction of amnioserosa cells during dorsal closure.

As germband retraction ends and dorsal closure begins (Bowne's stage 13), the embryo's dorsal surface is covered by the amnioserosa, a one-cell thick epithelium. As closure proceeds (stages 13-15), the adjacent epidermis (previously referred to as the germband) advances from the embryo's lateral flanks to seal over the amnioserosa, which dives inside the embryo. Dorsal closure has been extensively characterized in terms of its genetics, cell-shape changes, and tissue-level mechanics [4,5,24,70]. Laser microsurgery played a large role in the latter and established critical roles for three coordinated processes [4,5]: an adhesive interaction between approaching flanks of epidermis; contraction of a supracellular 'purse-string' along the amnioserosa-epidermis boundary; and apical constriction of amnioserosa cells. Similar instances of apical constriction occur

in gastrulation and neurulation [71,72]. In each case, a subgroup of epithelial cells contracts their apical surfaces while expanding in the apical-basal direction. When viewed in cross-section, the constricting cells take on a wedge-shaped morphology. Such constriction contributes substantial force for dorsal closure [4], and is the subject of our analysis here.

Our goal is to test, validate and eliminate alternative models for how the tension for contraction is carried in the amnioserosa cells. In general, epithelial sheets have been modeled as 2D cellular foams, *i.e.*, a network of tensile cell-cell interfaces [46,55,60]. The cytoplasm, as well as apical and basal surfaces, is treated as passive, incompressible media. Like in many epithelia, amnioserosa cells have their actin cytoskeletons organized cortically – largely in circumferential microfilament bundles. This organization is ubiquitously assumed to yield concentrated tensile forces along cell-cell interfaces. Whether this assumption is stated explicitly [13] or not [5], it is often used to estimate relative tensions based on the angles at cell triple junctions. We will first consider if this is an accurate model of the cells or if they behave more like a continuous sheet. Upon showing that not all of the tensile stress is located at the cell-cell interfaces, we will investigate other possible tension-carrying structures.

4.3 Experimental Methods

4.3.1 Fly strains and microscopy

The primary strain of *Drosophila melanogaster* used in this study is ubi-DE-Cad-GFP [38] (Kyoto Drosophila Genetic Resource Center). This strain ubiquitously

expresses a cadherin-GFP chimera that labels epithelial cell junctions. A few experiments use the strain sGMCA [5] (gift from D P Kiehart), which expresses a GFP-moesin construct that labels filamentous actin. For imaging and ablation, fly embryos were dechorionated in a 50% bleach solution, immersed in halocarbon oil 27 (Sigma-Aldrich, St Louis, MO), and sandwiched between a cover glass and an oxygen-permeable membrane (YSI, Yellow Spring, OH) [73]. Images were captured on a Zeiss LSM410 laser-scanning confocal microscope (inverted) with a 40×, 1.3 NA oil-immersion objective and 488 nm excitation. The scanning times were 2-8 s per frame and 15.74 ms per kymograph line.

4.3.2 Laser microsurgery

Ablations were performed with the third harmonic (355 nm) of a Q-switched Nd:YAG laser (5-ns pulsewidth, Continuum Minilite II, Santa Clara, CA). This laser was coupled into the Zeiss LSM410 with independent beam steering for simultaneous ablation and imaging [73]. The pulse energy was just high enough (2-3× threshold) to ensure consistent single-pulse ablation. This energy varied with the embryo stage and tissue – 1.16 ± 0.25 μJ for amnioserosa cells in stage 13 and 3.33 ± 0.91 μJ for these cells in stage 14 – due to differences in depth below the embryo's vitelline membrane – 2.3 ± 1.7 versus 16.4 ± 6.1 μm, respectively.

4.3.3 Image analysis

All image processing was performed with ImageJ (NIH, Bethesda, MD), using both built in and custom plug-ins.

4.3.4 Finite-element modeling

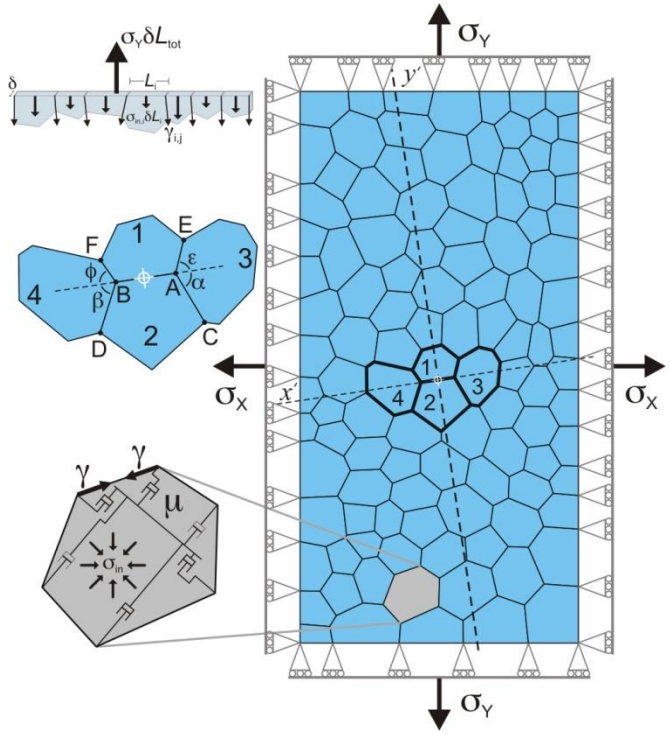

Figure 4.1. As appears in [6]. Cell-level finite-element representation of an epithelium: (*upper inset*) force balance along one edge of a cell patch; (*middle*) the local wound geometry; and (*lower*) the model for each cell.

We simulated the response to laser hole-drilling using custom-written, cell-level finite-element models [45,46]. As shown in Figure 4.1, an epithelium is modeled as a two-dimensional patch of tightly packed cells. Each cell is a polygon with edges representing cell-cell interfaces and nodes at cellular triple junctions. In the base model, each cell has three mechanical contributors. First, each cell-cell interface has a tension, γ. This tension represents both contraction of circumferential microfilament bundles and a tangential equivalent for cell-cell adhesion [49]. Second, each cell has a system of internal dashpots sized to model a uniform equivalent viscosity, μ [45]. This effective viscosity represents deformability of the cytoplasm and its embedded cytoskeletal

networks. Third, each cell is subject to an area constraint that yields an internal, in-plane, and isotropic cell stress σ_{in}. This stress encompasses both pressure from the incompressibility of cytoplasm and in-plane apical/basal tensions from the cortical cytoskeleton [50].

Although this base model exhibits system-level viscoelastic behavior [47,51], the full recoil kinematics are only reproduced by adding explicit viscoelastic rods – either along cell edges or as a pre-stressed intracellular mesh. These rods are necessary because the experiments involve very high strain rates, 1-5 s^{-1}. Previous uses of the base model focused on normal morphogenetic movements in which strain rates are < 0.5 h^{-1} [48,52].

A simulated epithelium also requires appropriate boundary conditions including constraints that keep the patch rectangular and constant external stresses σ_x and σ_y that are applied via external forces (Figure 4.1). These forces represent the far-field stress in the embryo, *i.e.*, the forces on the patch from cells outside the patch. This far-field stress is a major determinant of epithelial thickness [50] and of the simulated recoil behavior.

Computationally, the dynamic behavior of the model is described by [46]

$$(1/\Delta t)\mathbf{C} \cdot \Delta\mathbf{u} = \mathbf{f}, \tag{4.1}$$

which assumes low Reynolds number conditions. In this equation, Δt is a time step, **C** is the damping matrix, $\Delta\mathbf{u}$ is a vector of incremental node displacements, and **f** is a vector that represents the nonviscous forces acting on each node. **C** and **f** are calculated from the current cellular geometry. This system of equations is augmented by applicable constraints using Lagrange multipliers (including each σ_{in} for the cell area constraints).

The augmented system of equations is solved at each time step to yield values for the Lagrange multipliers and incremental displacements $\Delta\mathbf{u}$. The node positions are

updated and the process repeated, allowing the potential accumulation of large deformations. The model also allows cells to rearrange by changing the topology of the node connections when a cell edge becomes shorter than a given threshold [46].

4.4 Results and Discussion

4.4.1 Characterization of damage caused by hole-drilling

Before addressing questions of epithelial mechanics, we need to establish the extent of damage caused by hole-drilling. Figure 4.2 shows two examples of hole-drilling in the amnioserosa. The initial hole in the epithelium is marked by a similar hole in the embryo's overlying vitelling membrane (*e.g.*, the dark region with a hyper-flourescent ring in Figure 4.2*E*). This hole in the vitelline membrane is bound to a glue layer that holds the embryo onto the coverslip, limiting the membrane to only small amounts of expansion and preventing material from flowing in or out. In the absence of this glue layer, ablated embryos tend to lose material through any hole in the vitelline membrane. The hole apparent in Figure 4.2*E* is elliptical with semi-minor and semi-major axes of 0.50 and 0.75 μm – approximately one-tenth the size of a typical cell. In contrast to the hole in the vitelline, the hole in the epithelium rapidly expands.

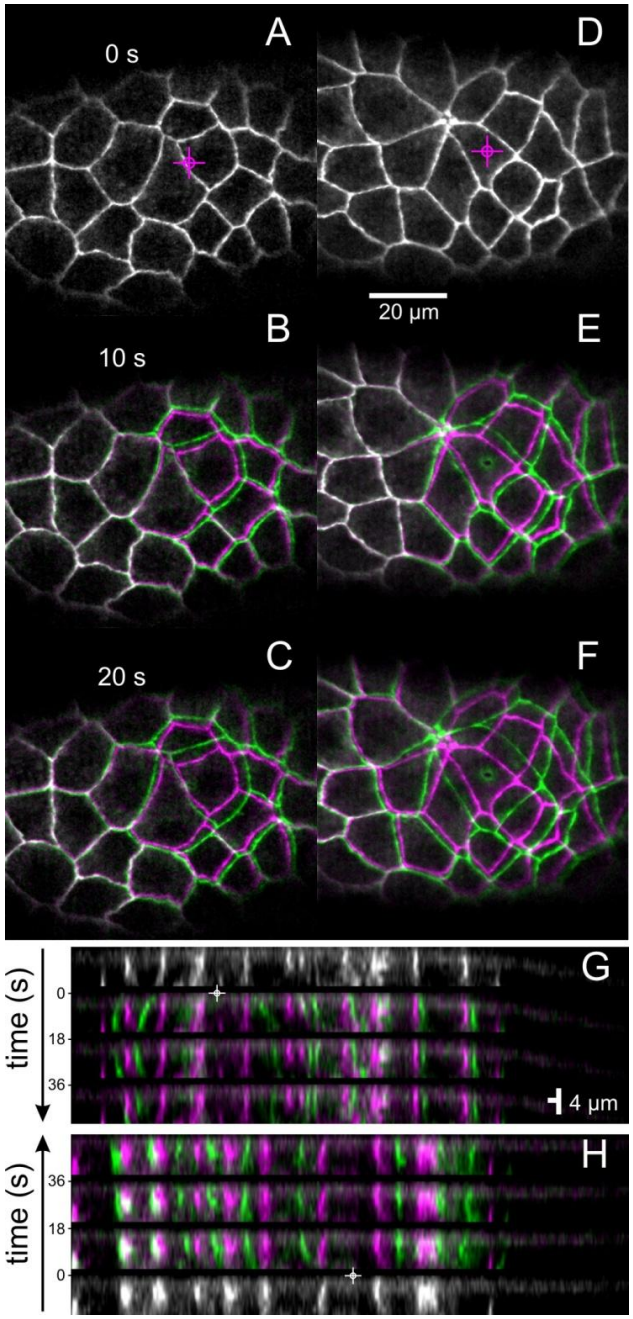

Figure 4.2. As appears in [1]. Mechanical response of the amnioserosa to single-pulse laser ablation. (*A*)-(*C*) Confocal images taken before, 10 s, and 20 s after ablation. The post-ablation images are overlays comparing the cell border positions before (magenta) and after (green) ablation. The laser was targeted to the cell edge under the crosshairs in *A*. (*D*)-(*F*) A similar series in which the laser targets a single cell's apical surface. For each image, anterior is to the right. (*G*), (*H*) Time-lapse cross-sectional images through the amnioserosa (dorsal up). Cell borders appear as nearly vertical bright lines. The crosshairs mark the time and location of ablation. The cross-sections in (*G*) were collected dorsal-to-ventral, so time increases as one goes down a single image. The cross-sections in (*H*) were collected ventral-to-dorsal, so time increases as one goes up a single image. The shear seen in (*G*) is reversed in (*H*), so the apparent shear is from the time delay and not from shear in the recoil.

Next we want to ensure that we are cutting through the entire epithelium. During dorsal closure the amnioserosa thickens, going from an average thickness of ~5 μm to an average thickness of ~7 μm. If we are only cutting through part of the cell, the part that was ablated should recoil much faster than the rest of the cell. Any portion that remains unablated would need to tear before recoiling. To evaluate if we are truly ablating through the tissue, we examined the wounds in cross-section (Figure 4.2*G, H*). There is some apparent shear in the first cross-section image after wounding (Figure 4.2*G*), but this is just an artifact from the motion of the tissue during the time it takes to collect an image at each successive depth. The apparent shear is reversed when the cross-sections are collected from bottom to top (Figure 4.2*H*). The magnitudes of the slopes of the apparent shear vary no more between the two imaging directions than the magnitudes vary between samples taken in the same direction. The lack of significant shear indicates that our laser protocol creates a hole clean through the epithelium, allowing the apical and basal surfaces to both move freely.

4.4.2 Investigating tissue response to a wound

Next we consider how the wounds expand. Figure 4.3 shows postablation changes in area for the ablated cells and their neighboring cells. The ablated cells expand by up to 90% in 20-60 s. After this point of maximum expansion, the neighboring cells begin to move back towards the ablation site as healing commences. In contrast, the neighboring cells initially maintain a nearly constant area (within ±6% in the first 10 s). At longer times, adjacent cells may increase or decrease in area, but these changes are mostly consistent with the pre-ablation trend for each cell. The only strong exception is for cells

at the endpoints of an ablated edge (*e.g.*, cell 3 in Figure 4.3*A*). Regardless of pre-ablation behavior, these cells tend to shrink ~10% over 30 s.

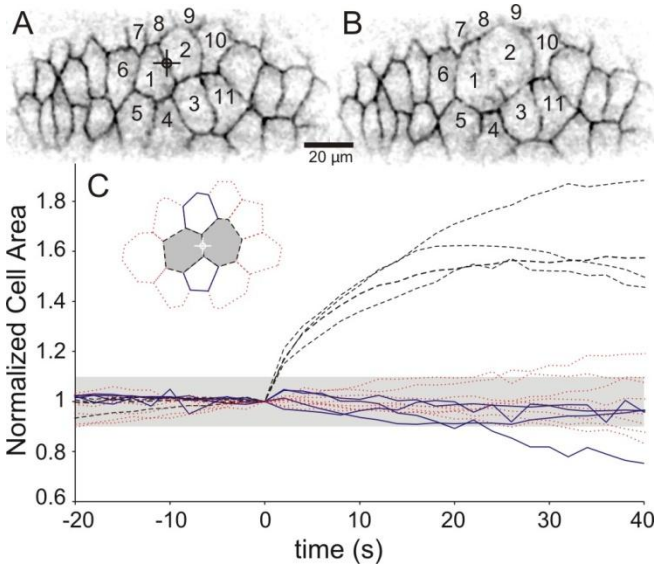

Figure 4.3. As appears in [6]. Experimental results for laser hole-drilling. (A and B) Confocal fluorescent images (inverted) of an embryonic epithelium before and 30 s after ablation at the targeted crosshairs. (C) Changes in the normalized apical surface area of nearby cells. In the graphical legend, the border of each cell type matches its line in the plot: (dashed) cells directly sharing the ablated border (*e.g.*, cells 1 and 2); (solid) nearest neighbor cells (*e.g.*, cells 3 and 8); and (dotted) next-nearest neighbors (*e.g.*, cells 4-7 and 9-11). The plot compiles results from four experiments. The lightly-shaded region marks area changes of ± 10%.

Since cells are mostly water, they should be incompressible, and thus maintain constant volume; however, the experimental results go a step further. The cells around a wound change shape, but maintain a nearly constant planform area, as if subject to a constraint on apical surface area (or volume and height). This constraint does not apply beyond the initial recoil, but is a reasonable approximation during the relatively short timescales (<10 s) needed to model the recoils from hole-drilling. It is also consistent with our previous observation that recoiling cells do not shear normal to the epithelial plane.

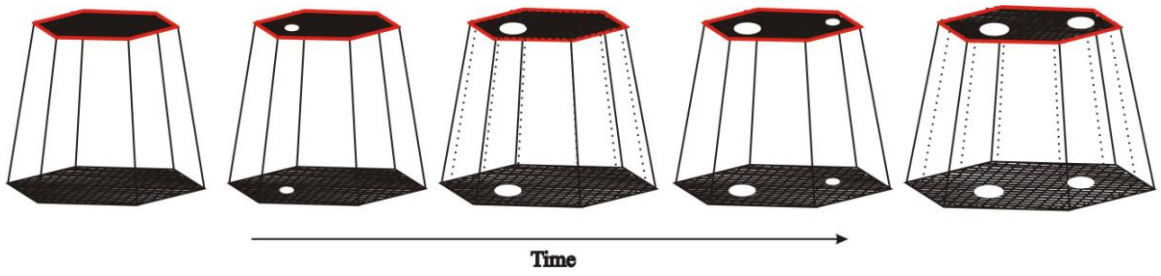

Figure 4.4. Schematic of a double hole-drilling experiment in a single cell. Red line represents the apical actomyosin belt, while the meshes represent the actomyosin meshes on the apical and basal surfaces. The first panel shows the cell pre-ablation. The second panel shows the cell immediately after the first ablation, and the third after that wound has expanded. The fourth panel shows the cell immediately after the second ablation, and the fifth after the cell has expanded from that wound.

To determine the extent to which ablation releases tension in the epithelium, we performed a series of double wounding experiments (Figure 4.4). The second ablation occurs as the initial recoil slows to a halt. If ablation releases the tension in the entire epithelium, then we would expect no recoil from the second ablation. To verify that no recoil occurs once the tension has been released, we performed a second ablation that targets the same location as the first, and, as expected, there was no recoil (N=2). We then looked at second ablations in adjacent cells and even at a different location in the same cell(s); there was always a second recoil (N=13 and 16 respectively). Thus, the wound does not stop expanding because tension relaxes across the epithelium, and ablating a hole is not equivalent to releasing tension across an entire ablated cell.

4.4.3 Tension-carrying structures

To determine if the tensile stress is limited to the intercellular interfaces, Dr. Xiaoyan Ma performed single-pulse laser ablation of the stage 13 amnioserosa at various subcellular locations. Strong recoils occur regardless of whether the wound is targeted to a cell edge (Figure 4.2*A*-*C*) or the cell center (Figure 4.2*D*-*F*). Apparently, and in contrast

to common assumptions [5,13,46], tension is not limited to the actin-rich apical belts around each cell.

To further investigate cell-center wounds, we moved the ablation focus perpendicular to the plane of the epithelium – allowing us to search for additional spatial constraints along the depth of the cell. Strong recoils occurred whenever the laser cut a cell's apical surface – regardless of whether it also cut the basal surface (*N*=16, Table 4.1). Recoils did not occur when the laser cut just the vitelline membrane. Thus, cell-center tension is carried by structures within a few μm of the apical surface. These structures are not specifically associated with the nucleus because strong recoils occurred regardless of whether the nucleus was targeted or not (*N*=5 and 8, respectively).

Table 4.1. As appears in [1]. Results from ablation experiments in which the laser was focused a given distance above the cell's adherens junctions. For each distance, the table compiles the fraction of experiments in which the basal surface was cut and/or recoil was observed.

Distance above adherens junctions	Basal surface cut	Recoil observed
4 μm	4/5	5/5
5 μm	1/3	3/3
6 μm	1/3	3/3
7 μm	0/2	1/2
8 μm	0/3	1/3

In addition to the circumferential microfilaments, amnioserosa cells have an apical actin network. Others have reported transient apical accumulations of actin and myosin in amnioserosa cells, especially those that dive out of the epithelial plane early [5,69,74]. Similar accumulations are evident in Figure 4.5*A*, which shows confocal images from basal, middle, and apical planes of the amnioserosa in a GFP-moesin embryo. In the middle plane, one can see the actin-rich belts along cell edges. In the apical plane, the cell centers are more fluorescent and the cell borders are covered with a

carpet of very mobile, actin-based projections. The basal surface also has actin-based projections, but they are not as mobile.

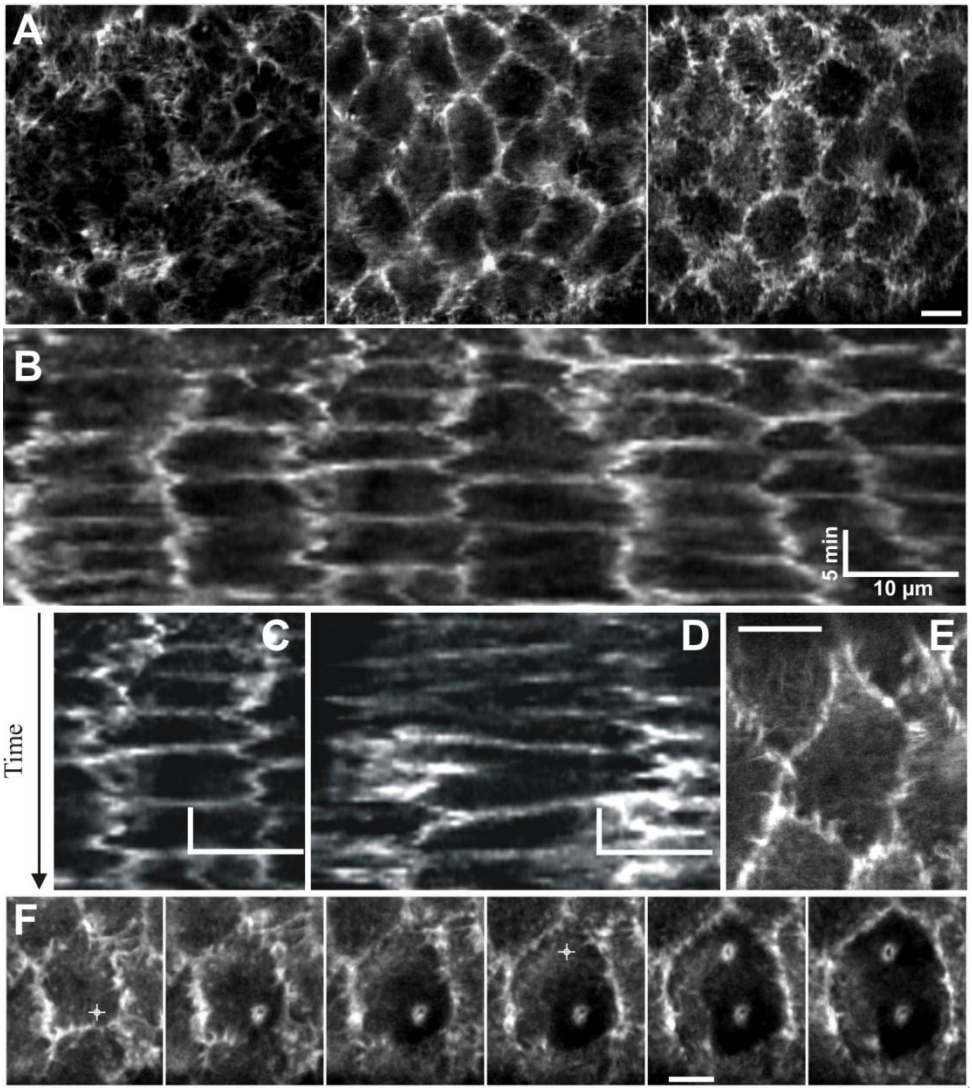

Figure 4 5. Modified from [1]. The apical actin network in GFP-moesin embryos. (*A*) Confocal fluorescent images of amnioserosa cells taken in different imaging planes (from left to right): basal, middle, and apical. (*B*) Long-time kymograph of contractile waves coupled to actin accumulations in the amnioserosa (time on the vertical axis). (*C*) Kymograph of a horizontal line across the cell in (*E*). (*D*) Kymograph of a vertical line across the cell in (*E*). (*F*) Time series of apical-plane images during a double wounding experiment. Ablation targets the crosshairs just after the first and fourth images (12 s between images). Each horizontal scale bar is 10 µm and all vertical scale bars are 5 minutes. Time always increases down the kymographs.

In time-lapse images of the apical surface, one can even see traveling contraction waves coupled to apical actin accumulations. This coupling is apparent in long-time

kymographs of the amnioseorsa (Figure 4.5*B-D*). The vertical lines correspond to cell edges that staircase back and forth with time. The turning points of this movement match up with bright horizontal lines, *i.e.*, transient local increases in actin. The overall effect makes the kymograph look like a ladder. The wave speed and period are approximately 0.2 μm/s and 200-300 s.

To investigate the role of the apical network in the recoil mechanics, we performed a double-wounding experiment on a GFP-moesin embryo (Figure 4.5*F*). By 24 s after the first ablation, there is a clear hole in the apical actin network (dark region around the hyper-fluorescent mark on the vitelline). This hole is ~10 μm across – larger than the laser spot, but smaller than a cell. Just as in Figure 4.2, the edges of the ablated cell have recoiled away from the wound site. At 48 s after the first ablation, we ablate a different location in the same cell. There is an immediate second recoil and formation of a second hole in the actin network. These results, combined with the correlation of actin accumulation and cellular contraction, point to the apical actin network as the carrier of cell-center stress.

4.4.4 Modeling

Others in my lab and collaborators looked at modeling the amnioserosa using a finite-element model and our experimental data [6]. We observed that apical area is constrained on short time scales (10 s) and that cells do not shear as they recoil. These observations justify modeling the initial recoil of cells using only two dimensions. Initial recoils from hole-drilling could be reproduced with a simple model – cells with constant

volume, an effective cytoplasmic viscosity, uniform tension along all cell-cell interfaces, and viscoelastic elements along cell-cell interfaces.

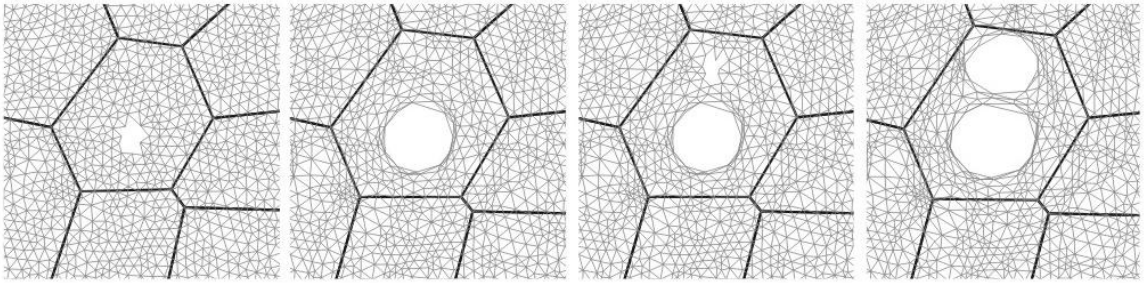

Figure 4.6. As appears in [6]. Simulated recoil in a cell subjected to two successive wounds. The second panel represents the equilibrium state reached after the first ablation; the fourth panel is the new equilibrium state after the second ablation. In terms of area, the second expansion is ~35% as large as the first.

To model double wounds in a single cell, however, an explicit model of the in-plane, intracellular cytoskeleton is required. This was accomplished by adding general viscoelastic rods (a Kelvin and Maxwell element in parallel) as a pre-stressed intracellular mesh (Figure 4.6). To best match both the long term behavior of the recoils and the double wound experiments the mesh is pre-stressed to approximately the internal cell stress.

4.5 Conclusions

Taking all of the experimental results into account, the mechanics of apical constriction in dorsal closure can be summarized as follows: the amnioserosa more closely resembles a continuous sheet than a network of tensile edges; tensile stress is carried by both circumferential actin and the apical actin network. The modeling also

confirms that the increasing expansion produced by successive wounds in a single cell is due to increasing damage to a pre-stressed, intracellular, viscoelastic network.

CHAPTER 5

SUMMARY AND CONCLUSIONS

In the preceding chapters we considered two important issues in understanding the physics of development: identifying which epithelial tissues contribute mechanically to a coordinated movement and determining the subcellular tension distributions in such a tissue. Though many of our results are specific to the particular movements and stages studied, the methods can be used to understand additional systems. In Chapter 1, we introduced the basic physics and biology of epithelial cells. We also gave a brief overview of the development of the *Drosophila* embryo, our chosen model organism, focusing on two stages: germband retraction and dorsal closure. Both of these stages involve the coordinated movements of two epithelial tissues: the germband (also called the lateral epidermis) and the amnioserosa.

Prior work done to understand the mechanical interactions between these tissues during germband retraction has been contradictory. The cell and tissue shapes and movements have been characterized [13,53] and used, along with the assumption that cellular tensions are carried along cell edges, to conclude that amnioserosa cells must pull on the germband [13]. Other research used the phenotypes of a mutant strain in which the amnioserosa undergoes premature apoptosis and germband retraction fails to conclude that the amnioserosa's necessity is limited to signaling. The primary result driving this conclusion was the partial recovery of germband retraction in these mutants through overexpression of a protein not found in the amnioserosa. On the other hand, in dorsal

closure, the mechanical, as well as biochemical, interactions between these same two tissues have been well characterized [4,5,24,70]. Dorsal closure occurs due to a combination of physical causes: an intracellular purse-string; zipping as the opposing sides of the germband approach each other; and contractile forces from the amnioserosa as the apical surfaces of its cells constrict. Here, in this dissertation, I have used a combination of laser microsurgery experiments and finite-element simulations to further delineate the mechanical interactions within and between the germband and amnioserosa. For germband retraction, we addressed the contradictions highlighted above. For dorsal closure, we analyzed the subcellular distribution of tension in the amnioserosa that leads to these cells' apical constriction.

Chapter 2 covers laser microsurgery experiments conducted on the germband and amnioserosa during germband retraction. We conducted three sets of microsurgery experiments: linear incisions in the germband; small to extremely large ablations of the amnioserosa; and incisions that isolate patches of germband cells. Through these experiments we showed the following:

- The amnioserosa does play a mechanical role in retraction, but does not mechanically interact with all germband segments. Its direct mechanical influence is limited to those around the curve.
- When germband cells are isolated from surrounding cells they maintain their shape. Thus, germband cells have a mechanism to at least hold their shape after removal of external forces. On the other hand, when ablation of the amnioserosa is destructive enough to halt germband retraction, germband cells on the ventral side of the embryo actually decrease in

aspect ratio. Together these two results suggest that this loss of aspect ratio is not due to a sudden absence of force from the amnioserosa.

- Cell elongation along the curve of the germband and furrow formation between germband segments are insufficient to uncurl the germband during retraction; both occur normally after destruction of an amnioserosa flank, but these embryos still fail to retract.
- Segments of the germband do not behave uniformly. Unlike the rest of the tissue, segments around the curve of the germband respond more anisotropically to line cuts, fade away even in large patches in the patch-isolation experiments, and continue to have cell elongation even when retraction fails due to ablation of the amnioserosa.

Chapter 3 discusses the use of finite-element simulations to further understand differences among germband segments regarding autonomous cell elongation and external stress anisotropy. The model defines cells as viscous and pressure-filled polygons with edges that have a defined active tension in parallel with viscoelastic rod elements. Autonomous elongation was simulated by a planar cell polarity in edge tensions, where edge tensions were varied by orientation so that stress-free elongation would be in the direction of polarization. Cell elongation was also impacted by anisotropic stress applied to the edges of simulated cell sheets. We investigated a large swath of parameter space for anisotropic external stress and cell polarizations. We determined the region of this parameter space that best fit each segment for three experimental results: pre-ablaion cell shape in terms of a composite cell's κ (square root of the ratio of the principal area moments); and the aspect ratio of maximally expanded

wounds following linear incisions made in two perpendicular directions, $\kappa_{w,y}$ and $\kappa_{w,x}$. Applying a χ^2 test to the fits between the segmental results for experiments and models, we are able to conclude:

- Cell polarization acts against the external anisotropy in most, if not all, segments.
- Segments for which cell elongation occurs along the direction of highest anisotropic stress are mostly around the curve of the germband (A1, A4, A5, A6, A7, and A9). Only in these segments is the direction of greatest stress consistent with a pulling force from the amnioserosa (Figure 5.1).
- In the remaining segments, cell elongation occurs along the direction of polarization (Figure 5.1).

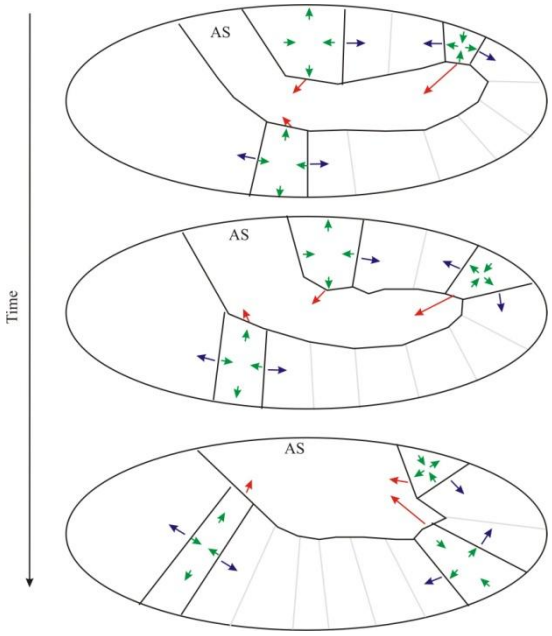

Figure 5.1. Model of germband retraction. Forces on segments T1, A5, and A8 are illustrated. The green arrows indicate forces internal to the segment, blue arrows represent forces from neighboring segments, and red arrows indicate forces on the segments from the amnioserosa. Many of the changes in the germband can occur autonomously, but a pulling force from the amnioserosa helps segments successfully travel around the bend in the tissue.

A more complete model can be pieced together from the simulations by using some of the results from Chapter 2 – in particular cell elongation after the destruction of a lateral amnioserosa flank. Cells in segment A5 elongate normally after this type of ablation, while those in segment A2 become less elongated. After ablation in segment A5, the principle external stress direction should be along the direction of its neighboring segments, since it is unable to retract but the tissue continues to shorten as furrows deepen. Despite this change in principle stress direction, the cells in A5 elongate along essentially the same direction as in unablated embryos. One possible explanation is that autonomous cell elongation is mechanically triggered to align with the direction of least stress. If we then consider the cells in A2, they would also experience an increased force along the direction of neighboring segments. This could be sufficient to decrease the aspect ratio of the cells as the anisotropic stress works against their attempts to elongate towards the amnioserosa. In the future, this should be probed further by investigating cell elongation in embryos where the amnioserosa undergoes premature apoptosis in combination with a similar modeling routine. Repeating this process in the same mutants when premature apoptosis is blocked biochemically, would be of additional interest, by indicating if the mechanics of the amnioserosa are preserved.

The final chapter, Chapter 4, changes gears to consider the subcellular distribution of tension in amnioserosa cells as they apically constrict during dorsal closure. By ablating sub-micron holes through the full thickness of the epithelium, we identified the force carrying locations within amnioserosa cells. By comparing the recoils of cell center and cell edge wounds, Dr. Xiaoyan Ma showed that tensile stress in the amnioserosa was not confined to cell edges as previously assumed. This led to my work investigating other

potential tension carrying structures in these cells. First, double wounding experiments showed that tension released by wounding the amnioserosa is local. Second, by varying the focal plane of ablation, I was able to wound either the full thickness of an amnioserosa cell, the vitelline membrane and the cell's apical surface, or only the vitelline membrane. Whenever the apical surface was cut, regardless of whether the basal surface was cut, surrounding cells recoiled from the wound, indicating that tension is carried close to the cells' apical surface. By examining a transgenic fly strain that fluorescently labels filamentous actin, we observed an actin mesh on both the basal and apical surfaces. The apical mesh was far more dynamic than that on the basal surface and showed increased actin concentration that correlated with the pulsed apical constrictions. Furthermore, the labeled actin mesh in these flies provided a visualization of subcellular holes in this mesh due to ablation. Double-wounding experiments in these flies showed that one ablation did not release all of the apical tension in the wounded cell; a second wound to a different part of a wounded cell again induced a mechanical response. These double-wounding experiments were only reproduced by finite-element simulations that included a pre-stressed, intracellular, viscoelastic mesh. Thus, tensile stress is carried by both the medial apical actin mesh as well as the circumferential apical actin belt. This combination causes the tissue to act more like a continuous sheet than a network of tensile edges.

This dissertation has furthered our understanding of the physical interactions that lead to proper development in *Drosophila* embryos, both by characterizing the interactions between two tissues that lead to their cohesive motion and by considering where tension is carried in cells constricting their apical surface. In addition, it has also

shown how laser microsurgery and finite element models can be used to study other morphogenetic movements. It has also questioned the validity of a general assumption that tension is carried along cell-cell interfaces. This work should provide a framework for interpreting future work on genetic mutations that interfere with dorsal closure and germband retraction. A deeper understanding of the importance of mechanical interactions for development will eventually lead to an understanding of how cells use genetics and biochemical signaling to create the mechanical environment necessary for proper development.

REFERENCES

[1] X. Ma, H.E. Lynch, P.C. Scully, and M.S. Hutson, "Probing embryonic tissue mechanics with laser hole drilling," *Physical biology*, vol. 6, p. 036004, 2009.

[2] T. Yeung et al., "Effects of substrate stiffness on cell morphology, cytoskeletal structure, and adhesion," *Cell motility and the cytoskeleton*, vol. 60, no. 1, pp. 24-34, 2004.

[3] M. Bownes, "A photographic study of development in the living embryo of *Drosophila melanogaster*," *Journal of embryology and experimental morphology*, vol. 33, no. 3, pp. 789-801, 1975.

[4] M.S. Hutson et al., "Forces for morphogenesis investigated with laser microsurgery and quantitative modeling," *Science*, vol. 300, no. 5616, p. 145, 2003.

[5] D.P. Kiehart, C.G. Galbraith, K.A. Edwards, W.L. Rickoll, and R.A. Montague, "Multiple forces contribute to cell sheet morphogenesis for dorsal closure in *Drosophila*," *The Journal of cell biology*, vol. 149, no. 2, pp. 471-490, 2000.

[6] M.S. Hutson et al., "Combining laser microsurgery and finite element modeling to assess cell-level epithelial mechanics," *Biophysical journal*, vol. 97, no. 12, pp. 3075-3085, 2009.

[7] Gabor Forgacs and Stuart A Newman, *Biological Physics of the Developing Embryo*. Cambridge: Cambridge University Press, 2005.

[8] Bruce Alberts et al., *Molecular Biology of the Cell*, 4th ed. New York: Garland Science, 2002.

[9] J.R. Sellers, "Regulation of cytoplasmic and smooth muscle myosin," *Current opinion in cell biology*, vol. 3, no. 1, pp. 98-104, 1991.

[10] T. Lecuit, P.F. Lenne, and E. Munro, "Force generation, transmission, and integration during cell and tissue morphogenesis," *Annual review of cell and developmental biology*, vol. 27, pp. 157-184, 2011.

[11] A.M. Mateus and A.M. Arias, "Patterned Cell Adhesion Associated with Tissue Deformations during Dorsal Closure in *Drosophila*," *PloS one*, vol. 6, no. 11, p. e27159, 2011.

[12] J.M. van der Meer and L.F. Jaffe, "Elemental composition of the perivitelline fluid in early *Drosophila* embryos," *Developmental Biology*, vol. 95, no. 1, pp. 249-252, 1983.

[13] F. Schöck and N. Perrimon, "Cellular processes associated with germ band retraction in *Drosophila*," *Developmental biology*, vol. 248, no. 1, pp. 29-39, 2002.

[14] Volker Hartenstein, *Atlas of Drosophila Development*. Plainview, NY: Cold Spring Harbor Labortory Press, 1993.

[15] C.W. Larsen, E. Hirst, C. Alexandre, and J.P. Vincent, "Segment boundary formation in *Drosophila* embryos," *Development*, vol. 130, no. 23, pp. 5625-5635, 2003.

[16] M.L. Lamka and H.D. Lipshitz, "Role of the amnioserosa in germ band retraction of the *Drosophila melanogaster* embryo," *Developmental biology*, vol. 214, no. 1, pp. 102-112, 1999.

[17] L.H. Frank and C. Rushlow, "A group of genes required for maintenance of the amnioserosa tissue in *Drosophila*," *Development*, vol. 122, no. 5, pp. 1343-1352, 1996.

[18] A. Scuderi and A. Letsou, "Amnioserosa is required for dorsal closure in *Drosophila*," *Developmental dynamics*, vol. 232, no. 3, pp. 791-800, 2005.

[19] A. Kumar and GV Shivashankar, "Mechanical Force Alters Morphogenetic Movements and Segmental Gene Expression Patterns during *Drosophila* Embryogenesis," *PloS one*, vol. 7, no. 3, p. e33089, 2012.

[20] K. Broadie, H. Skaer, and M. Bate, "Whole-embryo culture of *Drosophila*: development of embryonic tissues in vitro," *Development Genes and Evolution*, vol. 201, no. 6, pp. 364-375, 1992.

[21] B.H. Reed, R. Wilk, F. Schöck, and H.D. Lipshitz, "Integrin-dependent apposition of *Drosophila* extraembryonic membranes promotes morphogenesis and prevents anoikis," *Current biology*, vol. 14, no. 5, pp. 372-380, 2004.

[22] M. Leptin, T. Bogaert, R. Lehmann, and M. Wilcox, "The function of PS integrins during *Drosophila* embryogenesis," *Cell*, vol. 56, no. 3, pp. 401-408, 1989.

[23] F. Schöck and N. Perrimon, "Retraction of the *Drosophila* germ band requires cell-matrix interaction," *Genes \& development*, vol. 17, no. 5, p. 597, 2003.

[24] A. Rodriguez-Diaz et al., "Actomyosin purse strings: renewable resources that make morphogenesis robust and resilient," *HFSP journal*, vol. 2, no. 4, pp. 220-237, 2008.

[25] C. Henderson, "The Application of Boltzmann's Superposition Theory to Materials Exhibiting Reversible β Flow," *Proceedings of the Royal Society of London. Series A. Mathematical and Physical Sciences*, vol. 206, no. 1084, pp. 72-86, 1951.

[26] R M Christensen, *Theory of Viscoelasticity*, 2nd ed. New York: Academic Press, 1982.

[27] Andreas R Bausch, Florian Ziemann, Alexei A Boulbitch, Ken Jacobson, and Erich Sackmann, "Local Measurement of Viscoelastic Parameters of Adherent Cell Surfaces by Magnetic Bead Microrheometry," *Biophysical Journal*, vol. 75, pp. 2038-2049, 1998.

[28] P A Valberg and J P Butler, "Magnetic Particle Motions within Living Cells," *Biophysical Journal*, vol. 52, pp. 537-550, 1987.

[29] Anthony H B de Vries, Bea E Krenn, Roel van Driel, and Johannes S Kanger, "Micro Magnetic Tweezers for Nanomanipulation Inside Living Cells," *Biophysical Journal*, vol. 88, pp. 2137-2144, 2005.

[30] Alexander Ya Malkin and Avraam I Isayev, *Rheology - Concepts, Methods, & Applications*. Toronto: Chem Tec Publishing, 2006.

[31] Guillaume Lenormand, Emil Millet, Ben Fabry, James P Butler, and Jeffrey J Fredberg, "Linearity and time-scale invariance of the creep function in living cells," *Journal of the Royal Society Interface*, pp. 91-97, 2004.

[32] WB Amos and JG White, "How the confocal laser scanning microscope entered biological research," *Biology of the Cell*, vol. 95, no. 6, pp. 335-342, 2003.

[33] S.W. Paddock, "Confocal laser scanning microscopy," *Biotechniques,* vol. 27, pp. 992-1007, 1999.

[34] R. Heim, D.C. Prasher, and R.Y. Tsien, "Wavelength mutations and posttranslational autoxidation of green fluorescent protein," *Proceedings of the National Academy of Sciences*, vol. 91, no. 26, pp. 12501-12504, 1994.

[35] GJ Brakenhoff, HTM Van der Voort, EA Van Spronsen, WAM Linnemans, and N. Nanninga, "Three-dimensional chromatin distribution in neuroblastoma nuclei shown by confocal scanning laser microscopy," *Nature*, vol. 317, pp. 748-749, 1985.

[36] K. Carlsson et al., "Three-dimensional microscopy using a confocal laser scanning microscope," *Optics letters*, vol. 10, no. 2, pp. 53-55, 1985.

[37] JZ Young and F. Roberts, "A flying-spot microscope," *Nature*, no. 4241, p. 231, 1951.

[38] H. Oda and S. Tsukita, "Real-time imaging of cell-cell adherens junctions reveals that Drosophila mesoderm invagination begins with two phases of apical constriction of cells," *Journal of cell science*, vol. 114, no. 3, pp. 493-501, 2001.

[39] R.Y. Tsien, "The green fluorescent protein," *Annual review of biochemistry*, vol. 67, no. 1, pp. 509-544, 1998.

[40] R. Heim, A.B. Cubitt, and R.Y. Tsien, "Improved green fluorescence," *Nature*, vol. 373, no. 663-664, 1995.

[41] J. Colombelli, E.G. Reynaud, and E.H.K. Stelzer, "Investigating relaxation processes in cells and developing organisms: from cell ablation to cytoskeleton nanosurgery," *Methods in cell biology*, vol. 82, pp. 267-291, 2007.

[42] M.W. Berns et al., "Laser microsurgery in cell and developmental biology," *Science*, vol. 213, no. 4507, p. 505, 1981.

[43] B. Aigouy et al., "Cell flow reorients the axis of planar polarity in the wing epithelium of *Drosophila*," *Cell*, vol. 142, no. 5, pp. 773-786, 2010.

[44] D.N. Mashburn, H.E. Lynch, X. Ma, and M.S. Hutson, "Enabling user-guided segmentation and tracking of surface-labeled cells in time-lapse image sets of living tissues," *Cytometry Part A*, 2012.

[45] G.W. Brodland, D. Viens, and J.H. Veldhuis, "A new cell-based FE model for the mechanics of embryonic epithelia," *Computer Methods in Biomechanics and Biomedical Engineering*, vol. 10, no. 2, pp. 121-128, 2007.

[46] H.H. Chen and G.W. Brodland, "Cell-level finite element studies of viscous cells in planar aggregates," *Journal of biomechanical engineering*, vol. 122, p. 394, 2000.

[47] G.W. Brodland and C.J. Wiebe, "Mechanical effects of cell anisotropy on epithelia," *Computer Methods in Biomechanics and Biomedical Engineering*, vol. 7, no. 2, pp. 91-99, 2004.

[48] G.W. Brodland, D.I. Chen, J.H. Veldhuis, and others, "A cell-based constitutive model for embryonic epithelia and other planar aggregates of biological cells," *International journal of plasticity*, vol. 22, no. 6, pp. 965-995, 2006.

[49] G.W. Brodland, "The differential interfacial tension hypothesis (DITH): a comprehensive theory for the self-rearrangement of embryonic cells and tissues," *Journal of biomechanical engineering*, vol. 124, p. 188, 2002.

[50] X. Chen and G.W. Brodland, "Mechanical determinants of epithelium thickness in early-stage embryos," *Journal of the Mechanical Behavior of Biomedical Materials*, vol. 2, no. 5, pp. 494-501, 2009.

[51] X. Chen and G. Wayne Brodland, "Multi-scale finite element modeling allows the mechanics of amphibian neurulation to be elucidated," *Physical Biology*, vol. 5, p. 015003, 2008.

[52] J.H. Veldhuis, G.W. Brodland, C.J. Wiebe, and G.J. Bootsma, "Multiview robotic microscope reveals the in-plane kinematics of amphibian neurulation," *Annals of biomedical engineering*, vol. 33, no. 6, pp. 821-828, 2005.

[53] J A Campos-Ortega and V Hartenstein, *The Embryonic Development of Drosophila melanogaster*, 2nd ed. Berlin: Springer-Verlag, 1997.

[54] M. L. Richard Yip, Michele L. Lamka, and Howard D. Lipshitz, "Control of germ-band retraction in *Drosophila* by the zinc-finger protein HINDSIGHT," *Development*, vol. 124, pp. 2129-2141, 1997.

[55] M. Rauzi, P. Verant, T. Lecuit, and P.F. Lenne, "Nature and anisotropy of cortical forces orienting *Drosophila* tissue morphogenesis," *Nature cell biology*, vol. 10, no. 12, pp. 1401-1410, 2008.

[56] XG Peralta et al., "Upregulation of Forces and Morphogenic Asymmetries in Dorsal Closure during *Drosophila* Development," *Biophysical journal*, vol. 92, no. 7, pp. 2583-2596, 2007.

[57] I. Markovsky and S. Mahmoodi, "Least-squares contour alignment," *Signal Processing Letters, IEEE*, vol. 16, no. 1, pp. 41-44, 2009.

[58] L.A. Davidson, MA Koehl, R. Keller, and G.F. Oster, "How do sea urchins invaginate? Using biomechanics to distinguish between mechanisms of primary invagination," *Development*, vol. 121, no. 7, pp. 2005-2018, 1995.

[59] D.A. Clausi and G.W. Brodland, "Mechanical evaluation of theories of neurulation using computer simulations," *Development*, vol. 118, no. 3, pp. 1013-1023, 1993.

[60] F. Graner and J.A. Glazier, "Simulation of biological cell sorting using a two-dimensional extended Potts model," *Physical Review Letters*, vol. 69, no. 13, pp. 2013-2016, 1992.

[61] H. Honda, M. Tanemura, and T. Nagai, "A three-dimensional vertex dynamics cell model of space-filling polyhedra simulating cell behavior in a cell aggregate," *Journal of theoretical biology*, vol. 226, no. 4, pp. 439-453, 2004.

[62] G.M. Odell, G. Oster, P. Alberch, and B. Burnside, "The mechanical basis of morphogenesis: I. Epithelial folding and invagination," *Developmental biology*, vol. 85, no. 2, pp. 446-462, 1981.

[63] P.A. Pouille and E. Farge, "Hydrodynamic simulation of multicellular embryo invagination," *Physical biology*, vol. 5, p. 015005, 2008.

[64] M. Zajac, G.L. Jones, and J.A. Glazier, "Model of convergent extension in animal morphogenesis," *Physical Review Letters*, vol. 85, no. 9, pp. 2022-2025, 2000.

[65] LA Davidson, GF Oster, RE Keller, and MAR Koehl, "Measurements of Mechanical Properties of the Blastula Wall Reveal Which Hypothesized Mechanisms of Primary Invagination Are Physically Plausible in the Sea Urchin *Strongylocentrotus purpuratus*," *Developmental biology*, vol. 209, no. 2, pp. 221-238, 1999.

[66] R. Farhadifar, J.C. Röper, B. Aigouy, S. Eaton, and F. Jülicher, "The influence of cell mechanics, cell-cell interactions, and proliferation on epithelial packing," *Current Biology*, vol. 17, no. 24, pp. 2095-2104, 2007.

[67] S. Kumar et al., "Viscoelastic retraction of single living stress fibers and its impact on cell shape, cytoskeletal organization, and extracellular matrix mechanics," *Biophysical journal*, vol. 90, no. 10, p. 3762, 2006.

[68] W. Supatto et al., "*In vivo* modulation of morphogenetic movements in *Drosophila* embryos with femtosecond laser pulses," *Proceedings of the National Academy of Sciences of the United States of America*, vol. 102, no. 4, pp. 1047-1052, 2005.

[69] Y. Toyama, X.G. Peralta, A.R. Wells, D.P. Kiehart, and G.S. Edwards, "Apoptotic force and tissue dynamics during *Drosophila* embryogenesis," *Science Signalling*, vol. 321, no. 5896, p. 1683, 2008.

[70] A. Jacinto, S. Woolner, and P. Martin, "Dynamic Analysis of Dorsal Closure in *Drosophila*: From Genetics to Cell Biology," *Developmental cell*, vol. 3, no. 1, pp. 9-19, 2002.

[71] J.F. Colas and G.C. Schoenwolf, "Towards a cellular and molecular understanding of neurulation," *Developmental Dynamics*, vol. 221, no. 2, pp. 117-145, 2001.

[72] R. Keller, L.A. Davidson, and D.R. Shook, "How we are shaped: the biomechanics of gastrulation," *Differentiation*, vol. 71, no. 3, pp. 171-205, 2003.

[73] D.P. Kiehart et al., "Ultraviolet laser microbeam for dissection of Drosophila embryos," *Cell Biology: A Laboratory Handbook, 3rd ed., JE Celis, ed.(Elsevier Academic, 2006)*, pp. 87-103, 2006.

[74] C.C.F. Homem and M. Peifer, "Diaphanous regulates myosin and adherens junctions to control cell contractility and protrusive behavior during morphogenesis," *Development*, vol. 135, no. 6, pp. 1005-1018, 2008.